30

GNSS for Neutral Atmosphere and Severe Weather Monitoring

Hugues Brenot

Royal Belgian Institute for Space Aeronomy, Belgium

The ability of ground-based GNSS receivers to detect tropospheric water vapor was demonstrated during the early 1990s. Thanks to its stability in time and the high precision of its measurement of wet delays and integrated water vapor content (IWV), operating in any weather condition, GNSS became a key technique in operational meteorological observations. The increasing number of navigation satellites orbiting Earth and the continuous worldwide deployment of dense networks will enable more present and future GNSS applications in the field of atmospheric monitoring.

This chapter begins by giving a historical background of how geodetic study started to implement a strategy for correcting radio signal propagation through the neutral atmosphere. Following on from this, an overview of the process used to retrieve tropospheric parameters from geodetic software is given. The next section covers the details about the conversion of these GNSS parameters into wet delays and water vapor content. The use of GNSS meteorology for monitoring severe weather is then illustrated, highlighting the interest in very short-range forecasts, called nowcasting. Finally, future applications and synergy with other techniques is mentioned using derivative products.

To kick off the description of GNSS for severe weather monitoring, it seems appropriate to introduce why troposphere delay models are used in GNSS processing and to give a brief summary of how this technique appeared as a reference for the measurement of water vapor content. This state of the art of GNSS meteorology represents in as clear detail as possible the past achievements in GNSS research.

30.1 Retrieval of GNSS Tropospheric Parameters from Geodetic Software

Geodetic positioning solution by using GNSS requires a precise quantification of the phase delay propagation of signals transmitted by satellites through the atmosphere and received by ground-based receivers (see Parts A, B, D, and Chapters 27–29; [1, 2]). In its early stages, GPS technique concentrated essentially on correcting the effect of the ionosphere on radio wave path delays (e.g. the model of Klobuchar [3]; see Chapters 31, 32), but the tropospheric correction was quickly developed by geophysicists and geodesists [1, 4, 5]. In parallel, important progress for modeling these corrections was realized by the very long baseline interferometry (VLBI) research community, notably in calculating precise baselines and including, in theory, the tropospheric correction [6]. Even though calibration using atmospheric models were envisaged to improve the repeatability (or dispersion) of baseline calculations, the progress anticipated due to theoretical tropospheric corrections did not materialize at the end of the 1970s. Without the tropospheric correction of radio wave propagations, the interferometry technique was already allowing us centimetric precision (horizontal components only) for long intercontinental baselines [7–9].

In the early 1980s, the VLBI and GPS techniques started to successfully implement tropospheric parameters by employing mapping functions (e.g. [10, 11]), significantly improving the determination of baselines. In 1985, Davis et al. [12] validated the interest in atmospheric correction for VLBI long baseline estimates, using models or synoptic meteorological observations. By implementing atmospheric delay correction in calculations, the precision of VLBI vertical positioning became centimetric [13, 14]. Rather than using an atmospheric model to retrieve delays and improve positioning solutions, Ware and Hurst [15] decided to introduce a correction based on independent measurements of water vapor in calculations. In fact, as suggested by Bossler et al. [16] and Bender and Larden [17], Ware and Hurst applied simultaneous collocated IWV measurements from a water vapor radiometer (WVR). By combining the calculations of Bock et al. [18], based on the resolutions of phase ambiguities of signals

Position, Navigation, and Timing Technologies in the 21st Century: Integrated Satellite Navigation, Sensor Systems, and Civil Applications, Volume 1, First Edition. Edited by Y. T. Jade Morton, Frank van Diggelen, James J. Spilker Jr., and Bradford W. Parkinson.

(see Part B), with WVR measurements and ground pressure observations, Ware and Hurst showed that this correction can allow us a more precise estimation of baselines with improvement of the repeatability by a factor of 5. This result is confirmed by the works of Tralli et al. [19] on WVR calibration.

At the end of the 1980s, the analysis of phases of GPS signals became a way of estimating the trajectories of satellites with high precision ([20]; see Chapters 2,11, 62). However, the phase propagation is also one of the sources of error in positioning, among others, such as the quality of data records and its noise, clock parameters, phase ambiguities and carrier-phase cycle slip, multipath effect, parameterization of receivers, pattern of antenna, tide effect and oceanic and atmospheric loading, disruption of signals induced by the ionosphere and the neutral atmosphere; see Part B and Chapters 2, 10, 11, 31, 32, 47, and 62. Moreover, the use of phase observables, that is, linear combinations or double differences [21–25], enables the majority of errors in phase delay estimates to be avoided, especially the ones caused by clocks and the effect of the ionosphere. Such an analytical strategy permits us to consider that the only remaining correction (in regard to rectilinear propagation of a signal through empty space) is due to the neutral atmosphere. Considering a simplified model of the troposphere (formed by successive laterally homogeneous horizontal layers), this correction was characterized by Tralli and Lichten [26] as a zenith neutrosphere phase delay (ZND). This time delay of the signal propagation can be expressed as an equivalent path delay (the distance is simply obtained by multiplying by the speed of signal propagation, similar to light propagation). This path delay can be defined as the excess distance through which the signal propagates through empty space, in comparison to its propagation through the neutral atmosphere over the same time of propagation. Commonly, this path delay is called the zenith total delay (ZTD rather than ZND) of the neutral atmosphere or tropospheric delay, in a shortened and approximated version. This corrective distance is on the order of 2.5 m in the zenith direction for a site located at sea level. Considering its level of geodesic precision, Tralli and Lichten [26] planned that stand-alone GPS data processing can aspire to ZTD time series with uncertainties under 1%. Note that a universal format of GNSS data, compatible with any geodetic software, has been defined. It is called RINEX data (Receiver Independent Exchange Format; see Chapters 27 and 30, and [27]).

At the dawn of GNSS meteorology, Bevis et al. [28] announced GPS as a reliable instrument with which to measure the precipitable water of the troposphere (expressed in mm and equivalent to IWV in kg/m^2 with the assumption of a density of water equal to 1 g/cm^3). As a supplement to the achievements of the VLBI and GPS techniques, this work is based on preliminary results on the propagation of radio waves [12, 29, 30] and the conversion of its delay in IWV (by associating measurements of ground pressure and temperature). Therefore, GNSS techniques appeared to be a promising technique for atmospheric monitoring [31, 32]. A comparison with other techniques, like microwave WVR, radio sounding (RS), and VLBI, was then required to estimate the capacity of this technique in meteorology [28, 33–36], confirming valuable IWV estimates with an accuracy of 1–2 kg/m^2 (the same level of precision of conventional meteorological measurements).

Before giving further details about atmospheric monitoring, it is important to properly understand how tropospheric parameters are generated based on the disruption of GNSS signals. Geodetic software uses algorithms to adjust parameters. To retrieve meteorological observations, the strategy is to compare observations with theoretical values estimated from models. The residual differences between data records and theoretical models are minimized using least-squares adjustment, obtaining approximate tropospheric parameter solutions of this over-determined system.

30.1.1 Adjustment of ZTD

As an example, GPS satellites transmit two signals at frequencies L_1 (f_1 = 1.57542 GHz) and L_2 (f_2 = 1.22760 GHz). More details about GNSS signals are presented in Chapters 1–10. If noise and multipath effects are neglected, the simplified mathematical model of phase measurements (ϕ^i_{A,L_1} and ϕ^i_{A,L_2}), respectively, for L_1 and L_2, made by receiver A on satellite i (expressed in cycles) can be written as follows:

$$\phi^i_{A,L_1} = \frac{f_1}{c}\left(D^i_A + T^i_A - I^i_{A,L_1} + c\left(\Delta t^i - \Delta t_A\right)\right) + N^i_{A,L_1} \tag{30.1}$$

$$\phi^i_{A,L_2} = \frac{f_2}{c}\left(D^i_A + T^i_A - I^i_{A,L_2} + c\left(\Delta t^i - \Delta t_A\right)\right) + N^i_{A,L_2} \tag{30.2}$$

This model depends on the geometric distance between receiver A and satellite i (D^i_A), the tropospheric error (T^i_A), the dispersive ionospheric error (I^i_{A,L_1} or I^i_{A,L_2}), the receiver clock synchronization error (Δt_A), the satellite clock synchronization error (Δt^i), the phase ambiguity (integer number N^i_{A,L_1} or N^i_{A,L_2}), the considered carrier frequency f (f_1 or f_2), and the speed of electromagnetic waves (c).

The tropospheric error (T^i_A) is the path delay of the neutral atmosphere (called the tropospheric path delay). It is essentially induced by the thickness and the density of

the neutral atmosphere. This major contribution (generally about 90% of T_A^i at sea level), which depends on the altitude of the station and the fields of pressure and temperature, is called the hydrostatic delay [37]. For GNSS frequencies, another contribution to T_A^i exists. In fact, the molecule of water vapor has a dipolar moment that induces a delay effect on microwave propagation. This second contribution is called the wet delay [37]. The variability of T_A^i is principally controlled by the water vapor density through the atmospheric path travel (from 2% to 20% of T_A^i at sea level). A third contribution to tropospheric error can exist: this is the contribution of hydrometeors to the total delay of the neutral atmosphere [38–41]. This small contribution to the tropospheric path delay has a high variability (up to 3% of T_A^i).

The tropospheric error (T_A^i) can be converted to zenith tropospheric errors above a GNSS station A. Taking into account the variable composition and thickness of the neutral atmosphere for the direction of a satellite i (at azimuth α_i and elevation ϵ_i) visible from station A at time t, an approximation of the vertical tropospheric error ($T_A^{vertical}$) can be estimated using a mapping function MF:

$$T_A^i(t) \simeq T_A^{vertical}.MF(t, \alpha_i, \epsilon_i) \tag{30.3}$$

Over the last thirty years, geodesists and radiometeorologists have developed a range of models of atmospheric profiles and mapping functions allowing estimation of slant tropospheric delays for different elevations (ϵ). If the atmosphere was rigorously a plane without local tropospheric anisotropy around station A (troposphere formed by layers with a constant density), the simple mapping function (without azimuth dependency) is $\frac{1}{sin(\epsilon)}$. Nevertheless, in practice, for low elevations this simple function is generally not realistic [28, 42]. The challenge for implementing an improved mapping function was to correctly describe tropospheric delays under low elevation where these can reach several meters. Marini [11] has shown that the mapping function can be expressed by a formula based on fractions of the sine for a fixed elevation (ϵ):

$$MF(\epsilon) = \cfrac{1}{\sin\epsilon + \cfrac{a}{sin\,\epsilon + \cfrac{b}{\sin\epsilon + \cfrac{c}{\sin\epsilon + ...}}}} \tag{30.4}$$

where the coefficients a, b, c, ... are constant values or linear functions. In general, mapping functions are based on a truncation of Eq. 30.4. More complicated mapping functions have thus been introduced to convert slant delays into zenith delays more precisely taking into account the more important thickness of the troposphere at a low elevation and considering the error caused by straight line approximation [5, 10, 12, 43–60].

In the literature, the term $T_A^{vertical}$ (Eq. (30.3)) is more often referred to as ZTD. Neglecting the contribution of the hydrometeors to delay in GNSS processing, ZTD can be expressed by the summation of two terms (ZTD = ZHD + ZWD), where ZHD is the zenith hydrostatic delay, and ZWD is the zenith wet delay.

In term of meteorological applications, geodetic software can be useful for adjusting several ZTD per hour (sub-hourly process; see Haan et al., 2006). To extract the tropospheric error (T_A^i) from the phase measurements (ϕ_{A,L_1}^i, ϕ_{A,L_2}^i) four steps can be considered.

30.1.1.1 Step 1: The Ionosphere-Free Combination

The delay of the neutral atmosphere is a quantification of the decrease in the speed of propagation of the GNSS signal carrier phase; by contrast, the ionospheric delay quantifies how the speed of the propagation of the signal carrier phase increases through the ionosphere (this justifies the sign of the tropospheric and ionospheric corrections, as presented in Eqs. (30.1) and (30.2)). Unlike the ionosphere, the troposphere is non-dispersive for GNSS microwaves. Thus, the ionosphere-free (IF) combination allows us to remove the first order of ionospheric errors. Considering the simplified mathematical model of phase measurements presented in Eqs. 30.1 and 30.2, the IF combination is given by

$$\phi_{A,IF}^i = \eta\phi_{A,L_1}^i + \gamma\phi_{A,L_2}^i \tag{30.5}$$

with

$$\eta = \frac{f_1^2}{f_1^2 - f_2^2} \simeq 2.546 \tag{30.6}$$

and

$$\gamma = -\frac{f_1^2 f_2^2}{f_1^2 - f_2^2} \simeq -1.984 \tag{30.7}$$

If we neglect noise and multipath, the IF phase measurements $\phi_{A,IF}^i$ made by receiver A on satellite i can be expressed by

$$\phi_{A,IF}^i = \frac{f_1}{c}\left(D_A^i + T_A^i\right) + f_1\left(\Delta t^i - \Delta t_A\right) + N_{A,IF}^i \tag{30.8}$$

where f_1 is the frequency of L_1, and $N_{A,IF}^i$, the phase ambiguity of the IF combination (real number), can be expressed as

$$N_{A,IF}^i = \eta N_{A,L_1}^i + \gamma N_{A,L_2}^i \tag{30.9}$$

N^i_{A,L_1} and N^i_{A,L_2} are the respective ambiguities of L_1 and L_2 according to station A and satellite i, as given by Eqs. (30.1) and (30.2). More details about the principle of eliminating the ionospheric effect on the GNSS signal are presented by Spilker [61], King et al. [21], and Brunner and Gu [62]; see also Part B and Chapters 2, 10, 17, 28, and 31.

30.1.1.2 Step 2: Double Difference or Precise Point Positioning Technique

Two kinds of geodetic software can process the raw data (RINEX) recorded by ground-based GNSS receivers:

- Software using the double difference (DD) technique (see Chapter 19) and working on relative positioning based on the double differences of phase records (e.g. GAMIT developed by the MIT[1] or BERNESE developed by the AIUB[2]). For DD software, the use of an additional software (GLOBK/GLORG for GAMIT and ADDNED for BERNESE) is required in order to convert the relative position to an absolute position.
- Software using Precise Point Positioning technique (PPP; see Chapter 20 and Zumberge et al. [63]) to retrieve absolute positioning from direct processing of phase records in the RINEX data (e.g. GIPSY-OASIS software developed by JPL,[3] BERNESE software by the AIUB), EPOS 8 software developed by GFZ,[4] G-Nut/Tefnu software developed by GOP,[5] and NAPEOS software developed by ESA[6]).

For the example of GAMIT software [64], the DD technique allows us to remove clock errors from Eq. (30.8). In fact, considering two GNSS stations (A and B) and two satellites (i and j), we can form DDs ($\phi^{ij}_{A,IF}$) of the IF combination observations of Eq. 30.8:

$$\phi^{ij}_{AB,IF} = \frac{f_1}{c}\left(D^{ij}_{AB} + T^{ij}_{AB}\right) + N^{ij}_{AB,IF} \tag{30.10}$$

with the notations

$$*^{ij}_{AB,IF} = \left(*^i_{A,IF} - *^i_{B,IF}\right) - \left(*^j_{A,IF} - *^j_{B,IF}\right) \tag{30.11}$$

$$*^{ij}_{AB} = \left(*^i_A - *^i_B\right) - \left(*^j_A - *^j_B\right) \tag{30.12}$$

PPP software, like GIPSY-OASIS, works using a different approach (relating to satellite clocks and orbit solutions with autonomous processing for each station). The absolute positioning from PPP software is faster even though additional parameters for characterizing the clocks are resolved. The DD technique eliminates receiver and satellite clock errors. The relative positioning, for example, from GAMIT or BERNESE software, is more precise; however, the time of processing can be considerably impacted by the number of stations considered (quadratic progression).

30.1.1.3 Step 3: Positions and Resolution of Ambiguity to Extract Tropospheric Error

GNSS phase measurements, as described in Chapters 1–10, record the time evolution of the phases of signals, corresponding to a fractional part of the exact number of cycles existing along the path delay between satellite and receiver. This integer number of cycles is unknown, imparting an ambiguous character to the GNSS phase data records. The determination of ambiguities is necessary in order to retrieve the tropospheric parameter. A two-step approach can be considered. A first least-squares minimization is used to retrieve the ambiguities of signals emitted from satellites. These ambiguities take real values. If noise level and measurement errors are low, the ambiguities of the phases retrieved are close to integer values. Then, in a second least-squares minimization, ambiguities can be fixed to these integer values, allowing a proper adjustment of the other parameters (e.g. positions and tropospheric parameters). A reduction of the number of adjusted parameters ensures better quality of retrieval. With successful solutions of ambiguities, this second and final adjustment provides precise retrievals. In these two steps, a weight is applied to each parameter, and the adjustments follow more or less a random walk strategy until the stabilization of the solution [65]. Retrieval of GNSS parameters is an iterative process.

In practice, to be able to reconstruct information about the troposphere (T^{ij}_{AB}), it is necessary to simultaneously solve phase ambiguities (N^{ij}_{AB}) and positions characterized by the geometric term (D^{ij}_{AB}). This last term can be computed if the positions of stations A and B are assumed to be well known. This assumption is critical. For more details about geodetic positioning solutions, the reader can see Parts B and D and Chapters 27–28.

30.1.1.4 Step 4: ZTD Adjustment Using Geodetic Software and Mapping Function

Phase measurements (e.g. ϕ^i_A, ϕ^j_A, ϕ^i_B, ϕ^j_B) between each pair of stations and each pair of visible satellites are projected in the zenith direction using a mapping function (see Figure 30.1). Considering the combined tropospheric errors (e.g. T^{ij}_{AB}) established from the DDs of the mapped IF combinations (e.g. $\phi^{ij}_{AB,IF}$) or individual errors

1 MIT: Massachusetts Institute of Technology.
2 AIUB: Astronomisches Institut der Universität Bern.
3 JPL: Jet Propulsion Laboratory.
4 GFZ: German Research Centre for Geosciences.
5 GOP: Geodetic Observatory Pecny.
6 ESA: European Space Agency.

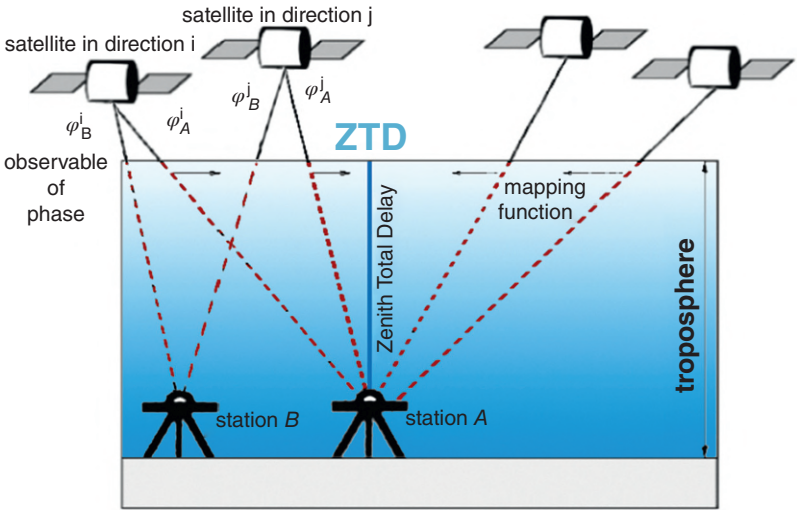

Figure 30.1 Illustration of the zenith total delay (ZTD) of the neutral atmosphere estimated using geodetic software (a time and space average considering every observable of phase). Note that ϕ^i_A corresponds to the following phase measurements (ϕ^i_{A,L_1}, ϕ^i_{A,L_2}).

(e.g. T^i_A, T^j_A, T^i_B, T^j_B) resolved in PPP, and using single mapped IF combinations (e.g. $\phi^i_{A,IF}$, $\phi^j_{A,IF}$, $\phi^i_{B,IF}$, $\phi^j_{B,IF}$), geodetic software allows us to make, for the selected stations, the adjustment to precise ZTD measurements.

For each baseline resolved in DD processing, the tropospheric error (T^{ij}_{AB}) is adjusted, which represents an adjustment of the difference in ZTD between stations A and B:

$$\begin{aligned} T^{ij}_{AB} &= \left(T^i_A - T^i_B\right) - \left(T^j_A - T^j_B\right) \\ &\simeq \left(ZTD_A - ZTD_B\right).\left(mf_{sym}(\epsilon_i) - mf_{sym}(\epsilon_j)\right) \end{aligned} \tag{30.13}$$

where

$$\begin{aligned} T^i_A &= ZTD_A.mf_{sym}(\epsilon_i) = L^i_{sym,A} \\ T^i_B &= ZTD_B.mf_{sym}(\epsilon_i) = L^i_{sym,B} \\ T^j_A &= ZTD_A.mf_{sym}(\epsilon_j) = L^j_{sym,A} \\ T^j_B &= ZTD_B.mf_{sym}(\epsilon_j) = L^j_{sym,B} \end{aligned} \tag{30.14}$$

The assessment of mean zenith total delays, for example, ZTD_A and ZTD_B at stations A and B, are processed considering the isotropic mapping function mf_{sym} (e.g. [58–60]), with spherical symmetry which depends on the elevations (e.g. elevations ϵ_i and ϵ_j of satellites i and j), and least-squares adjustments of tropospheric isotropic error delays for the direction of each visible satellite (e.g. $L^i_{sym,A}$, $L^i_{sym,B}$, $L^j_{sym,A}$, $L^j_{sym,B}$).

The final solutions of ZTD are constant values within a defined period (time window) and according to constraints applied in the adjustment process. For both, a setting in the calculations is required. To resolve these inversion solutions of ZTD, carrier-phase measurements of all visible satellites (e.g. ϕ^i_A, ϕ^j_A, ϕ^i_B, ϕ^j_B) are used in the calculations (space average) during a selected time window (time average). Resolutions of ambiguities and well-known positions of stations allow estimations of DD tropospheric error terms (e.g. via T^i_A, T^j_A, T^i_B, T^j_B) which are linked to the ZTD of each station. Considering k epochs of 30 s (intrinsic property of RINEX data recorder by receiver; note that there are receivers with other epoch rates such as 1 s) in the defined time window processed using geodetic software adjustments of ZTD (e.g. 15 min), and considering the number n_j of visible satellites at each epoch j, ZTD can be established by

$$\left| ZTD - \frac{1}{k}\sum_{j=1}^{k}\left(\frac{1}{n_j}\sum_{i=1}^{n_j}\frac{L_{sym}(\epsilon_i)}{mf_{sym}(\epsilon_i)}\right)\right| < \mu \tag{30.15}$$

In concrete terms, ZTD resolved using geodetic software is the result of a minimization process using μ criteria (e.g. $\mu = 10^{-4}$) during the inversion, leading to the adjustment of each $L_{sym}(\epsilon_i)$. ZTD is considered to be constant during the time window defined for the adjustment, and represents a precise average zenith tropospheric correction for each GNSS site of the selected network.

Note that, in general, even though ZTD is the tropospheric parameter retrieved by geodetic software, the adjustment is often based on another parameter. In fact, using a priori estimates of hydrostatic delays ($ZHD_{apriori}$ function of station altitude and ground pressure; see [37]), the adjustment focuses on wet delays ($ZTD_{retrieved} = ZWD_{adjusted} + ZHD_{apriori}$).

In combination with a mapping function of the troposphere, ZTD represents the isotropic contribution to the slant delays in the GNSS satellite direction.

30.1.2 Adjustment of Horizontal Delay Gradient

The number of visible satellites and the accuracy of slant delay measurements are critical for identifying the exact location of small-scale tropospheric structures. For this reason, a second tropospheric parameter has been introduced to the least-squares adjustment of geodetic software: the horizontal delay gradient [66–70]. Note that initially, horizontal gradients were introduced into the calculations in order to improve positioning solutions, showing a 15% increase in the repeatability [70] and a 25% improvement between wet delays from GNSS and WVR. Gradients are characterized by two components: G_{EW} and G_{NS} (respectively east-west and north-south). These represent a correction of phase residual projections depending on the elevations (ϵ_i) and azimuths (α_i) of visible satellites (anisotropic contribution). An inclined plane model of the troposphere (Figure 30.2) schematized by linear thickness and density variations is considered to define horizontal gradients during the adjustments of tropospheric parameters ([66, 71], section 1.3.4). The correction provided by gradients possesses its own mapping function mf_{az} 69]. The expression of azimuthal anisotropic contribution (L_{az}) to the reconstruction of slant delays depends on the satellite direction (elevation and azimuth).

The horizontal delay gradients are expressed by an equivalent additional distance. The convention of GAMIT geodetic software (Herring et al., 2010) is to adjust gradient components to an elevation of 10° (centimetric values). Using gradient mapping functions (mf_{az}), measurements of gradients can be converted into the zenith direction (millimetric values). In general, gradient components do not exceed 15 cm at 10°. This corresponds to a value of about 5 mm in the zenith direction. A positive value (of 5 cm at 10°, for example) of G_{EW} intuitively means that the slant delay at 10° of elevation in the east direction is 5 cm larger than the slant delay at 10° of elevation in the west direction (a slant delay at 10° of elevation is approximately 14 m at sea level). A cutoff angle of 10° is commonly used in calculations, and horizontal gradients characterize a conic zone of 50 km around the GNSS site (the hypothesis is that the water vapor density over 10 km is negligible). Considering a G_{EW} of 5 cm (at 10° elevation), the ZTD of a site located 25 km eastward at the same altitude is about 9 mm larger, representing an IWV that is about 1.5 kg/m^2 larger. A G_{EW} component (of 5 cm at 10° elevation) corresponds to a "zenith" gradient (at 90° elevation) of about 1.6 mm, which can be useful in improve imaging of the 2D field of ZTD from a network of stations.

ZTD and gradients can be resolved every 15 min. As for the estimation of ZTD, horizontal gradients also represent a time and space average adjustment according to the different visible satellites and phase measurements recorded by ground-based receivers over a defined period.

30.1.3 One-Way Post-Fit Residuals

The residual observation of phase delays retrieved by geodetic software, called one-way post-fit residuals (L_{res}), is available every 30 s for the direction of every visible satellite.

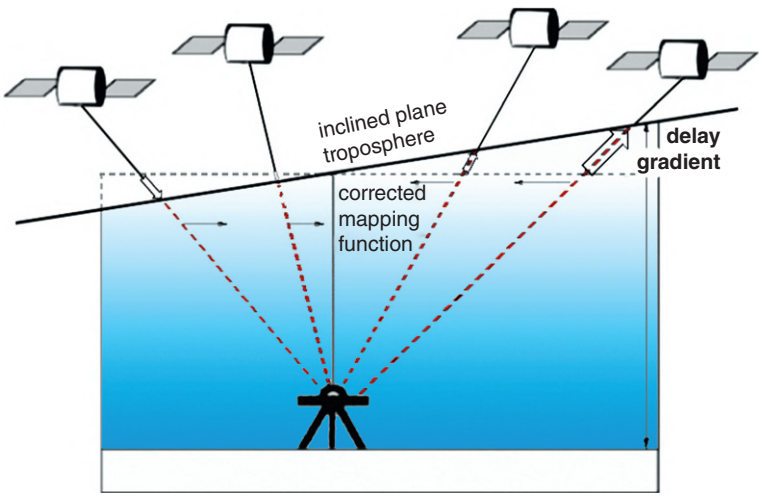

Figure 30.2 Illustration showing the implementation of horizontal delay gradients using geodetic software (anisotropic correction of phase observable residuals projected in the zenith direction).

The residuals contain any signal not modeled and absorbed by the adjustment of the first two tropospheric parameters (i.e. ZTD and gradients). In some cases, residuals can represent an additional contribution to the tropospheric delay or the multipath effect (see Chapters 22 and 34). For meteorological purposes, Champollion et al. [72] highlighted that the residuals can be interpreted as a small-scale local heterogeneousness of the water vapor field. Pany et al. [73] showed a 50% decrease of residuals when the water vapor content of the atmosphere is very low (i.e. in the dry summer season) in comparison to wet periods in autumn. Considering the hypothesis that the residuals are responsible for the third order of the tropospheric contribution, this can thus be added to the slant delay retrieved for the direction of a satellite, as illustrated in Figure 30.3. At the moment, it is not possible to generalize this assumption. Each situation should be considered individually. It is nevertheless possible to select GNSS sites that are very weakly influenced by multipath or that handle multipath using stacking methods. According to the work of Elósegui et al. [74], Iwabuchi et al. [75] present the use of MultiPath Stacking (MPS) functions as a way to correct residuals, improving GNSS observations at a low elevation [76]. The MPS functions accumulate, correlate, and identify residuals inferred with by multipath for each GNSS site and antenna. This avoids part of the non-tropospheric phenomena included in residuals and improves measurements of slant delays in satellite directions.

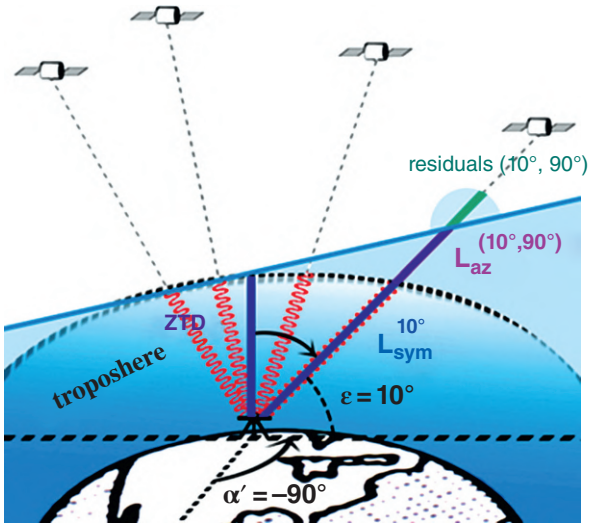

Figure 30.3 Illustration of the contribution of ZTD, delay gradients, and one-way post-fit residuals to slant delays for the direction of a satellite (10° elevation and 90° azimuth). Note that azimuth (α) is the angle relative to the north in the clockwise direction ($\alpha = 180^{\circ} + \alpha'$).

30.1.3.1 Other Sources of Unmodeled Error

The errors caused by the instabilities of the satellite clocks and the receivers are adjusted (or estimated using DD). The ionospheric delay is corrected using a linear combination. But there are other types of errors and influences that must be taken into account to reach millimetric positions (the fundamental base of GNSS meteorology). These sources of errors are singular, and each of them requires a specific strategy in GNSS processing:

- Generally, the electronic performance of receivers allows us to obtain data records with a satisfactory signal-to-noise ratio. The white noise (electronic origin) can be neglected. However, another source of error can be created by the multipath effect, which causes erroneous observations during data processing. In fact, some GNSS signals reach the antenna using a different path than the direct line of sight. These multipath records do not follow the principle of least time (Fermat's principle), and can be considered as the path travel reflected by vegetation or by the surrounding obstacles, close to the antenna [74]. When the elevation angle (between the horizon and a satellite) is over 15°, the least time of Fermat's principle (which signifies a spontaneous path with minimal energy) is very close to the straight line path (theoretically the minimal path travel). The combination of multipath with spontaneous path travels induced an erroneous mean delay recorded by a receiver. Multipath is a phenomenon linked to the geometry between the satellite, a reflector, and the antenna (see Chapters 22 and 34). This geometry varies with the progress of the satellite in its orbit. Over a sufficient observational period (about 12 h), satellite revolution can be described by an important range of positions related to an antenna. In that case, there is a good chance in considering, on average, a cancellation of the multipath effect. Note that during an interval of 6 h, a satellite can have traversed a whole hemisphere over a GNSS station. To average the errors introduced by multipath and estimate them, the observations should be processed for at least 6 to 12 h. However, in the case of monitoring of the atmosphere, the focus is on sub-hourly periods. For this reason, a strategy for the identification of multipath is applied in order to reject them from calculations using MPS functions, as shown by Shoji et al. [76]. On the other hand, models of antenna correction are required in order to improve GNSS tropospheric observations. Indeed, the reconstruction of slant delays can be more precise by using a PCV (phase center variation) model, defining the phase center variations according to the type of antenna used. The antenna corrections are determined from empirical models. Shoji et al. [76] show a post-treatment of tropospheric parameters. This improves slant delay

observations, according to the type of antenna considered using PCV models and MPS functions.

- The type of antenna must be specified in the calculations. Each antenna is characterized by the position of its phase center (the electromagnetic center of the antenna), which differs in accordance with the position of the antenna. Note that the position of the phase center changes over time. This variation depends on the frequency of the received signal (e.g. L_1 or L_2), on the satellite directions (azimuth and elevation). This is an intrinsic property of antenna (for more details, see Chapter 26; [77–79]).
- The errors in GNSS satellites orbits have a direct impact on the positioning solutions of the stations. The most precise orbits are required to retrieve the best positions. The best choice is the final orbits provided by the International GNSS Service (IGS) and implemented considering data from the permanent GNSS network (http://www.igs.org). IGS collects, distributes, and analyzes data from their permanent network. Products from IGS contain orbits of high quality, information on satellite clocks, parameters of orientation of Earth, and positions and speeds of permanent stations. IGS distributes a final solution of GNSS satellite orbits with high quality about two weeks after observations. With an average error of a few centimeters for orbits whose distance is greater than 20 000 km, the impact on the estimation of a baseline of about 1000 km is less than 1 cm. To minimize the error on absolute precise network positioning, Tregoning et al. [35] suggested considering estimations of very long baselines in calculations (more than 2000 km long). In such network processing, outputs about the quality of orbits can be obtained. The repeatability of baseline estimates on the basis of their length can also be studied. If the repeatability remains constant for all the lengths of lines, the chosen orbits are rather precise for the considered network. The use of less precise orbits (i.e. broadcasting signals for navigation) will require them to be adjusted in the least-squares process. More details are presented in Chapters 11, 40, and 62.
- The solid Earth tides are a source of error on positioning which needs to be corrected. Models of correction based on the analyses of tides (a theoretical model adjusted by gravimetric observations; c.f. VLBI and SLR) are used to retrieve a positioning solution. The applied model of the International Earth Rotation and Reference Systems Service (http://www.iers.org) considers the positions of the Sun and the Moon (see Chapters 27, 39, and 52). Note that other ground deformations, like oceanic and atmospheric loading, can also be considered to establish positioning solutions. Indeed, the masses of the ocean (current and ocean's tide) and of the atmosphere can deform continents.

30.1.4 Retrievals of Slant Total Delay of the Neutral Atmosphere

In the literature, the tropospheric error T_A^i (Eqs. 30.1 and 30.2) is called the slant total delay of the neutral atmosphere (STD). As presented in Section 30.1.1, GNSS phase measurements are ambiguous. For this reason, STD cannot be directly measured. Using geodetic software, a reconstruction of STD can be established considering the following three tropospheric parameters: (1) the ZTD (symmetric contribution), (2) the horizontal delay gradients (asymmetric contribution), and (3) the residuals (final adjustment for the direction of a defined satellite).

30.1.4.1 Contribution with Spherical Symmetry (L_{sym})

STD for the direction of a satellite i, as described by the tropospheric error T_A^i, is not directly available. The use of the tropospheric models and mapping functions is required to estimate STD. More details about these models (hydrostatic and wet contributions) and the formulation of atmospheric refractivity is presented in Section 30.2.

Considering ZTD measurements (see Section 30.1.1), the isotropic delay (L_{sym}) can be mapped using the hydrostatic and wet mapping functions, mf_{sym}^h and mf_{sym}^w, respectively (e.g. see [58–60]) for the direction of satellite i with elevation ϵ_i:

$$L_{sym}(\epsilon_i) = \mathrm{ZHD}_{\mathrm{apriori}} \cdot mf_{sym}^h(\epsilon_i) + \mathrm{ZWD}_{\mathrm{adjusted}} \cdot mf_{sym}^w(\epsilon_i) \quad (30.16)$$

This isotropic contribution to STD is independent of the azimuth α_i of the selected satellite, and can define a cone of path delay around a GNSS site (spherical symmetry). During the selected event shown Figure 30.4a, this contribution at 10° ($L_{sym}^{10^\circ} = L_{sym}(10)$; see Eq. 30.16) is about 14 m for the Château-Renard (CHRN) station (located at an altitude of 103 m a.s.l.). $L_{sym}^{10^\circ}$ takes values for a range of 0.24 m in less than 6 h.

30.1.4.2 Contribution with Azimuthal Asymmetry (L_{az})

A simple model of an inclined plane troposphere allows us to resolve horizontal delay gradients into two components, G_{EW} and G_{NS}. The first order of the anisotropic contribution to delays (L_{az}) induced by water vapor (and eventually hydrometeors) up to about 50 km around a GNSS site for the direction of the satellite i can be formulated depending on the elevation ϵ_i and azimuth α_i of this satellite:

$$L_{az}(\epsilon_i, \alpha_i) = mf_{az}(\epsilon_i) \cdot (G_{NS} m. \cos(\alpha_i) + G_{EW} \cdot \sin(\alpha_i)) \quad (30.17)$$

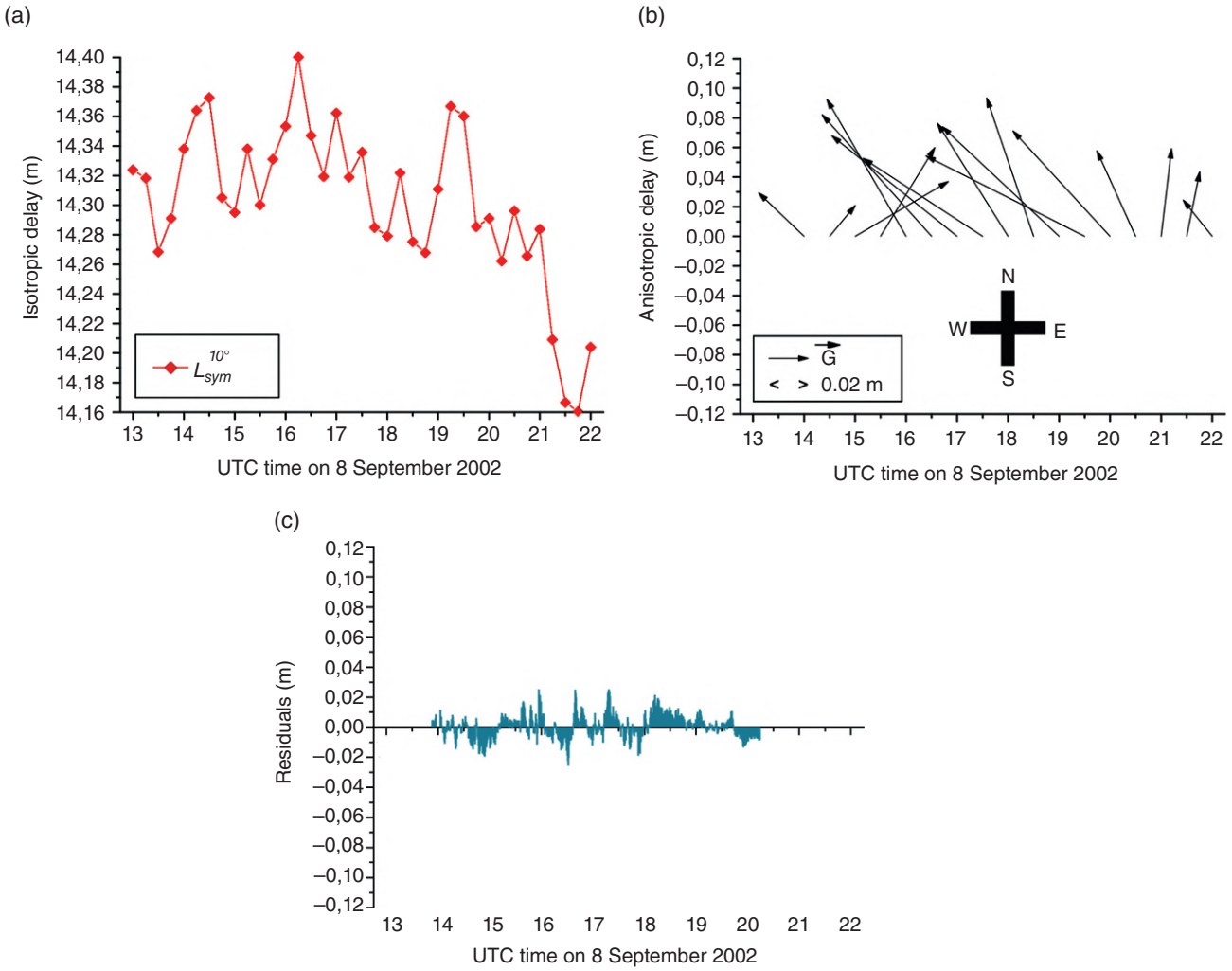

Figure 30.4 Tropospheric parameters measured at the Château-Renard (CHRN) station during the flash-flood event of 8–9 September 2002. (a) The isotropic delay (ZTD estimated every 15 min) is mapped at 10° $\left(L_{sym}^{10^\circ}\right)$. (b) The horizontal gradients $\vec{G}$ are retrieved at 10° elevation (every 30 min). (c) The residuals are provided every 30 s for the direction of the satellite PRN09 at the elevation ϵ and mapped at 10° $\left(L_{res}^{10^\circ}\right)$.

This expression for the anisotropic contribution to STD combines a mapping function (mf_{az}) which depends on the elevation ϵ_i and a constant C [69], with gradient components connected to the azimuth α_i (azimuthal asymmetry).

$$mf_{az}(\epsilon_i) = \frac{1}{sin\,(\epsilon_i).\,tan\,(\epsilon_i) + C} \tag{30.18}$$

The gradient components (G_{EW}, G_{NS}) are total. This means there is no dissociation between wet and hydrostatic gradients [69, 80]. In geodetic software, it is commonly considered that $C = 0.0032$ [57].

Figure 30.4b shows gradient components up to more than 0.10 m at 10° elevation.

30.1.4.3 Final Reconstruction of STD with Contribution of Residuals (L_{res})

The two tropospheric parameters adjusted using geodetic software are ZTD and horizontal gradients. These parameters allow us to reconstruct the STD for the direction of a satellite i with an elevation ϵ_i and an azimuth α_i, which is equivalent to the tropospheric error T_A^i of a station A. If a GNSS site is not subjected to multipath, the monitoring of small-scale tropospheric structures can be achieved with the following optimal reconstruction of STD, that is, the sum of L_{sym} (obtained from ZTD), L_{az} (obtained from horizontal gradient components), and L_{res} (residuals from the adjustment of ZTD and gradients):

$$\text{STD}\ (\epsilon_i, \alpha_i) = L_{sym}(\epsilon_i) + L_{az}(\epsilon_i, \alpha_i) + L_{res}(\epsilon_i, \alpha_i) \quad (30.19)$$

The post-fit phase residuals of the inversion calculation (L_{res}) performed using geodetic software can be considered as the third tropospheric parameter available. Values of L_{res} rarely exceed a few centimeters. Figure 30.4c show residuals up to about 0.03 m at 10° elevation $\left(L_{res}^{10^\circ} = L_{res} \cdot mf_{sym}(10^o) / mf_{sym}(\epsilon_i)\right)$. In practice, for some cases, these post-fit residuals cannot be only due to tropospheric effects. These can contain all the remaining unmodeled effects. Using an analysis of the PCV for the antenna of a station, non-tropospheric residuals can be avoided. From a meteorological point of view, the final STD reconstruction (with or without residuals) can be very useful in detecting convective cells or small-scale structures.

Figure 30.5 presents the slant delays measured every 30 s at the CHRN station. The time resolutions of ZTD and gradients are respectively 15 and 30 min. To obtain such a skyplot (STD retrieved using GAMIT software; Herring et al., 2010), ZTD and gradients components are interpolated following the 30 s time resolution of residuals (as recommended by Bob King from the Department of Earth, Atmospheric and Planetary Sciences of MIT). Thanks to the knowledge of the satellite trajectory on the same skyplot as the STDs (Figure 30.5), information about the direction of the tropospheric arc observed is provided. The trajectory of satellite PRN09 shows a scan of the sky from the west (at 14 h UTC) to the southeast (at 20 h UTC). The anisotropy of delay induced by water vapor is located on the northwestern side of the CHRN station.

30.1.5 Setting and Strategy to Retrieve Tropospheric Parameters

The strategy for obtaining tropospheric parameters depends on the type of application. In the case of severe weather monitoring, observations with high temporal resolution and variability are required. Because the reliability of residuals is quite unpredictable due to the multipath effect or other errors, high variability of ZTD and horizontal gradients, with low constraint, is recommended [81]. Because observations of the lower layers of the atmosphere are needed to understand weather events, GNSS processing for meteorology tries to consider low cutoff angles. For this reason, the choice of the mapping function can be critical. For mid-latitudes, the use of empirical mapping functions

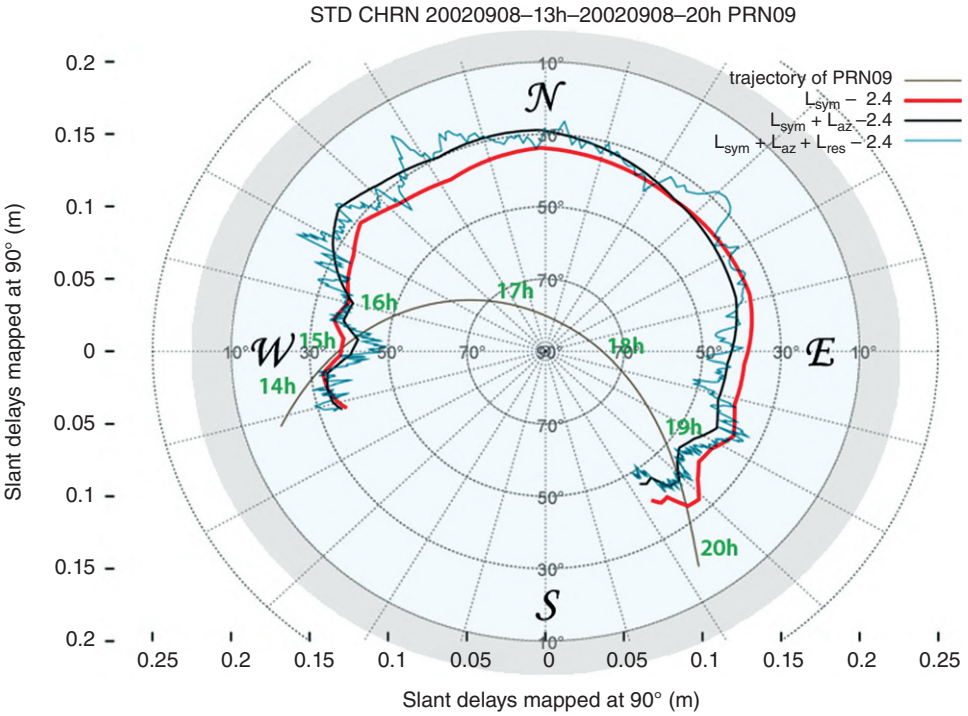

Figure 30.5 Contributions to slant delays (along the axes in black), for the direction of satellite PRN09 (trajectory in brown line; elevation in gray and azimuth described by cardinal points in black), mapped at 90° for CHRN station on 8 September 2002. The red line shows the isotropic contribution (L_{sym}), the black line the additional anisotropic contribution ($L_{sym} + L_{az}$), and the blue line the STD with residuals ($L_{sym} + L_{az} + L_{res}$). Note that for all these contributions, a delay of 2.4 m has been subtracted to show the variations of the slant delays more clearly.

(e.g. NMF or GMF) is sufficient for providing observations with a cutoff angle of 10° [59]. But for data processing for other latitudes or lower cutoff angles (down to 3°), mapping functions considering information about the troposphere are needed (e.g. VMF1 based on numerical weather model outputs; [60]).

Sessions of calculations are required to retrieve tropospheric parameters. To avoid the side effect in the time series of retrievals, a sliding window strategy needs to be applied. If you divide the duration of the session by 3, only the middle hours (corresponding to a third of the duration) are considered. This duration is a key parameter. Figure 30.6 illustrates two types of configurations used to retrieve daily ZTD and gradients with a time resolution of 30 min. When the embedded convection moved eastward (at noon on 9 September 2002; DOY 252), we can see the difference between the two types: (1) difference in the amplitude of ZTD and the time of the passage of the mesoscale convective system (MCS) over the CHRN station, (2) difference in the monitoring of the passage of the MCS using gradients. The recommendation for severe weather monitoring is the following: 6 sessions of 12 (for a time resolution 15 min) or 12 sessions of 6 h (for a time resolution of 5 min); see Brenot et al. [82] for the use of GNSS retrievals for nowcasting applications.

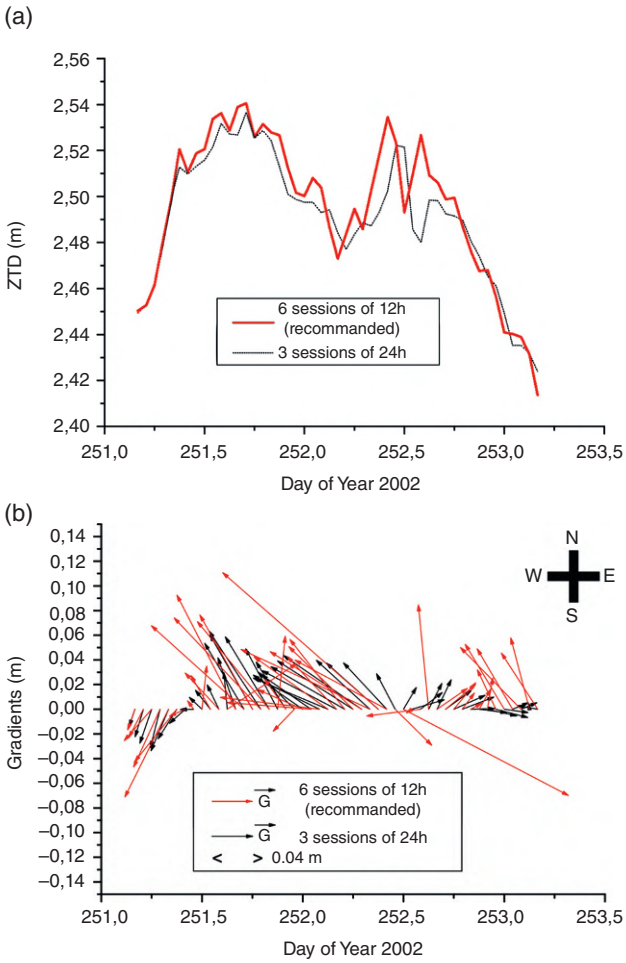

Figure 30.6 Time series of (a) ZTD, (b) gradients at CHRN station during the flash-flood event of 8–9 September 2002 over southeastern France. Two configurations of the sliding windows strategy are presented (six sessions of 12 h considering only the middle 4 h, and three sessions of 24 h considering only the middle 8 h).

Sensitivity to the geometry of network and settings (constraints, positioning solutions) in calculations have been tested by Brenot et al. [81]. Note that the mean latitude of the networks studied was about 45°N. The precision of ZTD can be estimated at 5–10 mm. For the gradient components, due to the distribution of satellites in the sky at 45°, the EW component has better precision than the NS one (respectively 5–15 mm and 10–20 mm at 10° elevation, which corresponds to 0.15–0.5 mm and 0.3–0.7 mm in the zenith direction). In other areas of the world (e.g. the Southern Hemisphere or close to the pole), the impact of the geometry of the GNSS satellite constellation on ZTD and gradients is certainly different, notably for the NS and EW components of the gradients.

A time resolution of 15 min is generally sufficient for monitoring events on a meteorological time scale. In the following section, an example of monitoring of severe weather situations will be presented using post-processed GNSS observations with GAMIT software.

Note that in the case of climatological studies, the strategy applied to measure tropospheric parameters (mainly ZTD) is different. The aim of such studies is to consider very stable time series. For this reason, three sessions of 24 h (still using a sliding window strategy to avoid issues at the beginning and the end of the session) with a time resolution of 30 min or 1 h is an adequate strategy.

30.2 Water Vapor Monitoring Using GNSS Technique

Measurements of water vapor content of the neutral atmosphere is a key parameter for the understanding and forecasts of the meteorological process (i.e. initiation of large-scale convection, mesoscale deep convection, and monitoring of the humidity field of the lower layer). A panel of studies describing the state of the art of operational techniques for water vapor retrievals is presented by Kämpfer [83]. This includes ground-based instruments (WVR, sun photometer, LiDAR, Fourier Transform InfraRed – FTIR – spectrometer), in situ methods (RS and airborne instruments), and remote sensing (IR, visible and microwave sensors). Each technique has its own limitations. Remote sensing allows

us global coverage, but no retrievals can be obtained during cloudy and rainy weather (for visible and IR sensors) or over land (for microwave sensors). During severe weather conditions, it is recognized that the coverage by terrestrial measurements (RS, sun photometer, LiDAR, FTIR spectrometer, Max-DOAS) is generally insufficient for correctly characterizing the three-dimensional water vapor field at the mesoscale. However, the GNSS technique has the ability to provide observations with a high temporal frequency (sub-hourly), operating in all weather conditions with an intrinsic stable method [84]. It is also relatively low cost in comparison to other instruments (especially by using already existing GNSS stations or by installing new GNSS stations which are less expensive than other instruments), as previously mentioned, making this technique very attractive, especially in terms of meteorological applications and network monitoring. This section presents the methodology for extracting water vapor content from delay measurements, slant wet delay, and slant IWV content for directional positioning of satellites.

30.2.1 Extractions of ZWD and IWV from GNSS ZTD

To understand how wet delay and water vapor content can be extracted, more details about the analytical expression for ZTD in L-Band radio signal propagation is required.

30.2.1.1 Analytical Expression for ZTD

$$\mathrm{ZTD} = 10^{-6}\int_{z_0}^{\infty} N \; dz = \mathrm{ZHD} + \mathrm{ZWD} + \mathrm{ZHmD} \tag{30.20}$$

where the z parameter is the vertical altitude, z_0 the altitude of the GNSS site, N the atmospheric refractivity, and ZHD, ZWD, and ZHmD are respectively the hydrostatic, wet, and hydrometeor contributions to the zenith path delay. The atmospheric refractivity can be expressed as

$$N = N_{hydrostatic} + N_{wet} + N_{hydrometeors} \tag{30.21}$$

The zenith path delay of the GNSS signal and the associated atmospheric refractivity are defined by three components, respectively – ZHD, ZWD, and ZHmD – and ($N_{hydrostatic}$, N_{wet}, $N_{hydrometeors}$).

ZHD represents the contribution of the total density of all gas in the neutral atmosphere to ZTD (including water vapor density) with the following expression:

$$\mathrm{ZHD} = 10^{-6}\int_{z_0}^{\infty} k_1 R_d \; \rho \; dz = 10^{-6}\int_{z_0}^{\infty} k_1 \frac{P}{T_v} \; dz \tag{30.22}$$

where ρ is the density of air; P the pressure; $R_d = (287.0586 \pm 0.0055)$ J/(kmol. K), the specific molar gas constant for dry air; T_v the virtual temperature; and k_1 an atmospheric refractivity coefficient. ZHD, which makes up the major part of ZTD, is about 2.3 m at sea level.

On the other hand, the major variation of ZTD is essentially driven by the water vapor content over a site (e.g. ZWD ranges from 0.05 m to 0.50 m at sea level). This specific additional contribution of water vapor to ZTD can be expressed as

$$\mathrm{ZWD} = 10^{-6}\int_{z_0}^{\infty}\left(k_2 R_w - k_1 R_d + \frac{k_3}{T} R_w\right)\rho_{wv}$$

$$dz = 10^{-6}\int_{L}\left(k_2'\frac{e}{T} + k_3\frac{e}{T^2}\right) \; dz \tag{30.23}$$

where ρ_{wv} is the density of water vapor; $R_w = (461.525 \pm 0.013)$ J/(kmol. K), the specific molar gas constant for water vapor; and e the partial pressure of water vapor. Because of its polar nature, water vapor has a density and a density-temperature term, which are respectively described by the refractivity coefficients k_2 and k_3. Note that $k_2' = k_2 - k_1\frac{R_d}{R_w}$.

Different estimations of k_1, k_2, and k_3 can be found in the following literature on this subject (e.g. [85–89]). Bevis et al. [90] revised data used by Hasegawa and Stokesberry [89], eliminated outliers, and provided mean values for $k_1 = (0.7760 \pm 0.0005)$ Pa/K, $k_2 = (0.704 \pm 0.022)$ Pa/K, $k_3 = (373900 \pm 1200)$ Pa/K^2, and $k_2' = (0.2213 \pm 0.0220)$ Pa/K. More recently, Rüeger (2002) recomputed the k_1 coefficient for air with a carbon dioxide content of 375 ppm (0.0375%), providing $k_1 = 0.77689$ Pa/K with a $N_{hydrostatic}$ accuracy of 0.02%. He also provided $k_2 = 0.712952$ Pa/K, $k_3 = 375463$ Pa/K^2, and $k_2' = 0.2297$ Pa/K. The accuracy of the water vapor component N_{wet} is 0.2%. Saastamoinen (1973, Part 2) [48] proposed an expression for k_1 as a function of pressure and temperature. Brenot et al. [41] adapted this expression for the frequency of GNSS signals:

$$k_1 = \chi\left(1 + \beta \; \frac{(P-e)}{T}\right) \tag{30.24}$$

with $\chi = 0.7755$ K/Pa and $\beta = 1.3 \; 10^{-7}$ K/Pa.

Note that for the expression of ZHD and ZWD, the compression factors can be assumed to be negligible [41].

ZHmD stands for the sporadic contribution of hydrometeors, that is, liquid (e.g. cloud and water rain) and solid water (e.g. pristine ice, snow, hailstones, and graupel), to ZTD. Generally neglected in the literature, it can be expressed as

$$\mathrm{ZHmD} = 10^{-6}\int_{z_0}^{\infty}(N_{lw} + N_{ice})\ dz = k_{lw}M_{lw} + k_{ice}M_{ice} \tag{30.25}$$

where N_{lw} and N_{ice} are respectively the atmospheric refractivity of liquid and solid water, and M_{lw} and M_{ice} are the mass content of the liquid and solid water particles per unit of air volume. Assuming that the densities of liquid and solid water are respectively equal to 1 g/cm^3 and 0.916 g/cm^3, the values of the coefficients k_{lw}(≈1.45) and k_{ice}(≈0.69) depend on the respective permittivities. Brenot et al. [41] present details about the temperature dependency of k_{lw} and an expression for k_{ice}. This study shows that the hydrometeor delay can be significant during rainfall events, notably with ZHmD values estimated up to 0.07 m during the flash-flood event which occurred on 8–9 September 2002 over southeastern France.

After this presentation of the analytical expression for ZTD, the assumptions considered by the GNSS technique for extracting ZWD and IWV can be properly described. Because the distribution of hydrometeors in the field of view of GNSS satellites is strongly limited in space and time, the mean contribution of hydrometeors (in satellite directions) to the mean ZTD measured above a site is neglected in the GNSS extraction of wet delay and water vapor content (respectively $\mathrm{ZWD_{GNSS}}$ and $\mathrm{IWV_{GNSS}}$).

30.2.1.2 GNSS Estimate of ZWD

In 1972, Saastamoinen [37] specified how to estimate the hydrostatic delay of the neutral atmosphere depending on the surface pressure P_s. Indeed, if the atmosphere is assumed to be in hydrostatic equilibrium, the hydrostatic delay (in meters) can be represented by the following expression [12, 91]:

$$\mathrm{ZHD}_{estimate} = 10^{-6}\frac{k_1 R_d P_s}{\mathrm{g_m}} \tag{30.26}$$

where $\mathrm{g_m}$ is the mean gravity of the atmospheric column above the site. Saastamoinen's expression for $\mathrm{g_m}$(1972) depends on the latitude λ and the altitude H a.s.l. (in meters):

$$\mathrm{g_m} = 9.784 \times (1 - 0.0026\cos(2\lambda) - 0.000000279\ H) \tag{30.27}$$

This formulation of Saastamoinen is commonly used in GNSS processing, easily allowing a priori estimation of the hydrostatic delay, simply with knowledge of the altitude of the GNSS site and assuming a standard estimation of the pressure with the hypsometric equation.

Vedel et al. [92] provide an alternative expression for the hydrostatic delay. This expression also considers an atmosphere in hydrostatic equilibrium and is based on the assumption that the temperature is constant in the column above the site (T_m):

$$\mathrm{ZHD}_{estimate} = 10^{-6}\frac{k_1 R_d P_s}{g(r)}\left\{1 + 2\frac{R_d T_m}{r\ g(r)} + 2\left(\frac{R_d T_m}{r\ g(r)}\right)^2\right\} \tag{30.28}$$

where r and $g(r)$ are the respective distances to the center of Earth ($r = r_0 + h_0$; in meters) and the acceleration due to gravity at the location of the GNSS site. h_0 is the altitude of the GNSS station above the geoid. The expression for $g(r)$ is as follows:

$$g(r) \approx g_0\left(\frac{r_0}{r}\right)^2 \tag{30.29}$$

g_0 can be derived using the procedures outlined in Vedel et al. [92]:

$$g_0 \approx g_e\left(1 + a_1\ \sin^2\lambda + a_2\ \sin^2 2\lambda\right) \tag{30.30}$$

with $g_e = 9.780356$ m/s^2, $a_1 = 5.2885\ 10^{-3}$, and $a_2 = -5.9\ 10^{-6}$.

r_0, the distance to the center of Earth from the projection of the GNSS site to the geoid surface, can be expressed as

$$r_0 \approx \frac{r_e}{\sqrt{\left(\frac{r_e}{r_p}\right)^2 \sin^2\lambda + \cos^2\lambda}} \tag{30.31}$$

where r_e (≈6378100 m) is the average equatorial radius, and r_p ($\approx r_e - 21500$ m) the average pole radius.

The last parameter required in order to estimate the hydrostatic delay with the formulation of Vedel et al. [92] is the mean temperature of the column above the GNSS site (T_m). The analytical expression for T_m is as follows [30]:

$$T_m = \frac{\int_{z_0}^{\infty}\frac{e}{T}\ dz}{\int_{z_0}^{\infty}\frac{e}{T^2}\ dz} \tag{30.32}$$

From a linear regression based on 8718 RSs (launched in the United States for latitudes between 27°N and 65°N), Bevis et al. [28] presented the following estimation of T_m as a function of the surface temperature T_s (in K):

$$T_m = 70.2 + 0.72\ T_s \tag{30.33}$$

For a station with a latitude $\lambda = 45$°N, an altitude $z_0 = 100$ m, a surface pressure $P_s = 101325$ Pa, and a surface temperature $T_s = 290$ K, $\mathrm{ZHD}_{estimate}$ from Vedel et al. [92] is about 2.315 m and 0.006 m higher than the value from [37].

Considering GNSS retrievals of the ZTD ($\mathrm{ZTD_{GNSS}}$) and the surface pressure (P_s) at the station, it is possible to estimate the zenith wet delay ($\mathrm{ZWD_{GNSS}}$):

$$\mathrm{ZWD_{GNSS}} = \mathrm{ZTD_{GNSS}} - \mathrm{ZHD}_{estimate} \tag{30.34}$$

30.2.1.3 GNSS Estimate of IWV

Hogg et al. [29] introduce a proportionality factor κ to connect IWV with ZWD:

$$\mathrm{IWV} = \int_{z_0}^{\infty} \rho_{wv}\ dz \approx \kappa\ .\ \mathrm{ZWD} \tag{30.35}$$

where ρ_{wv} is the water vapor density.

In 1987, Askne et Nordius [30] specified an expression for κ:

$$\kappa = \frac{10^8}{R_w\left(\frac{k_3}{T_m} + k_2'\right)} \tag{30.36}$$

The estimation of T_m from Bevis et al. [28], Eq. 30.33, can be introduced in the formulation of κ, Eq. 30.36, yielding the following GNSS estimate:

$$\mathrm{IWV_{GNSS}} = \kappa\ .\ \mathrm{ZWD_{GNSS}} \tag{30.37}$$

For a value of κ of about 167 kg/m^3, the conversion of 6 mm of ZWD corresponds to an IWV of about 1 kg/m^2. If there is no measurement of surface pressure and temperature at the GNSS site, the outputs from meteorological models can be considered to obtain these parameters, that is, P_s and T_m (see [93]). Commonly, meteorological applications consider precipitable water (expressed in millimeters) rather than the equivalent IWV (expressed in kg/m^2). The precipitable water is defined as the liquid equivalent of the total water vapor contained in an air column above a site [84].

30.2.1.4 Sensitivity and Validation of GNSS Wet Delays and Water Vapor Content

GNSS atmospheric measurements have been validated by comparisons with independent measurements and numerical weather prediction models [92–102]. The accuracies of $\mathrm{ZWD_{GNSS}}$ and $\mathrm{IWV_{GNSS}}$ extractions are generally very good, with respective values of less than 0.01 m and 1.5 kg/m^2. Using more than 15 years of GNSS ZTD retrievals for 28 worldwide sites, Van Malderen et al. [93] compare $\mathrm{IWV_{GNSS}}$ with coincident satellite IWV observations, together with sun photometer and/or radiosonde measurements. The mean biases of the different techniques compared to the GNSS estimates only vary between −0.3 to 0.5 kg/m^2 of IWV.

This accuracy is degraded during severe weather. Brenot et al. [41] use outputs from a non-hydrostatic high-resolution model (Méso-NH; see [103]) to test the sensitivity of GNSS estimates ($\mathrm{ZWD_{GNSS}}$ and $\mathrm{IWV_{GNSS}}$) during an extreme flood event. Results show that the conversion of Eq. 30.37 is pretty good (accuracy better than 0.3 kg/m^2). In the heart of the convective cells, the use of the hydrostatic formulation (to infer $\mathrm{ZHD}_{estimate}$) can lead to an overestimation of up to 0.018 m (a mean overestimation of less than 0.6 kg/m^2), and the simulated hydrometeor delays reach more than 0.07 m, showing a consequent overestimation of $\mathrm{ZWD_{GNSS}}$ (Eq. 30.34). The expression for the coefficient k_1, a function of pressure and temperature (Eq. 30.24), has also been tested, resulting in a mean overestimation of $\mathrm{IWV_{GNSS}}$ of about 0.4 kg/m^2 (from 0.15 kg/m^2 to 1 kg/m^2). It is important to mention that this study considers only simulations of ZTD. No simulations of slant delays for the directions of GNSS satellites have been considered to estimate the mean delay of hydrometeors contributing to ZTD and the mean overestimation of $\mathrm{ZHD}_{estimate}$. The real degradation of Eq. 30.34 is certainly diminished using slant records from the GNSS constellation.

30.2.2 GNSS Retrievals of SWD and SIWV

The final reconstruction of STD for a satellite i with elevation ϵ_i and azimuth α_i (Section 30.1.4) lays down the methodological base for retrieving the GNSS slant wet delay ($\mathrm{SWD_{GNSS}}$): (1) isotropic contribution from wet delay, (2) anisotropic contribution from wet gradients, and eventually (3) contribution from wet residuals,

$$\mathrm{SWD_{GNSS}}\ (\epsilon_i, \alpha_i) = L^w_{sym}(\epsilon_i) + L^w_{az}(\epsilon_i, \alpha_i) + L^w_{res}(\epsilon_i, \alpha_i) \tag{30.38}$$

The isotropic contribution from wet delay uses $\mathrm{ZWD_{GNSS}}$ from Eq. 30.34 and the wet mapping function mf^w_{sym} mentioned in Section 30.1.4.1:

$$L^w_{sym}(\epsilon_i) = \mathrm{ZWD_{GNSS}}\ .\ mf^w_{sym}(\epsilon_i) \tag{30.39}$$

The anisotropic contribution from wet gradients (L^w_{az}) is based on the total gradient (L_{az}), described in Section 30.1.4.2, and the subtraction of the hydrostatic gradient (L^h_{az}):

$$L^w_{az}(\epsilon_i, \alpha_i) = L_{az}(\epsilon_i, \alpha_i) - L^h_{az}(\epsilon_i, \alpha_i) \tag{30.40}$$

The expression for the hydrostatic gradient $L^h_{az}(\epsilon_i, \alpha_i)$ is the following:

$$L^h_{az}(\epsilon_i, \alpha_i) = mf^h_{az}(\epsilon_i)\ .\ \left(G^h_{NS}\ .\ cos\,(\alpha_i) + G^h_{EW}\ .\ sin\,(\alpha_i)\right) \tag{30.41}$$

Assuming an effective height of the gradients (scale height H) in the hydrostatic delay of about 13 km, the mapping function of the hydrostatic gradient (mf^h_{az}) can take the following expression for the elevation ϵ_i of satellite i:

$$mf^h_{az}(\epsilon_i) = \frac{1}{sin\,(\epsilon_i).\,tan\,(\epsilon_i) + C} \tag{30.42}$$

The value of C can be fixed to 0.0031 [69]. To obtain the components G^h_{NS} and G^h_{EW}, a characterization of the surface pressure field around the GNSS station is required. A hydrostatic gradient can be established by fitting a plane through the pressure measurements at each measurement epoch [72, 81]. From the pressure field near a GNSS site, the spatial variations of the hydrostatic delay per unit of distance (kilometers) in the north-south (Z^h_{NS}) and east-west (Z^h_{EW}) directions can be calculated (e.g. by using the hydrostatic formulation from Eq. 30.26 or Eq. 30.28). Note that if surface pressure measurements are not available, outputs from numerical weather prediction (NWP) can also be considered. Assuming an exponential law in the hydrostatic refractivity and considering the scale height of the gradients in the hydrostatic delays set to $H = 13$ km (as suggested by Chen and Herring [69]), the spatial variations of the hydrostatic delay can be converted to hydrostatic gradients [80, 104, 105]:

$$\begin{pmatrix} G^h_{NS} \\ G^h_{EW} \end{pmatrix} = H. \begin{pmatrix} Z^h_{NS} \\ Z^h_{EW} \end{pmatrix} \tag{30.43}$$

Time series of total, wet, and hydrostatic gradients have been worked out by Champollion et al. [72] and Brenot et al. [81].

The one-way post-fit residuals, as described Section 30.1.3, can be considered as a higher order of the tropospheric wet delay if a site is very weakly affected by multipath. In that case, we can assume the total residuals to be a wet contribution ($L^w_{res} = L_{res}$).

Finally, the GNSS slant IWV content retrieval ($\mathrm{SIWV_{GNSS}}$) can be simply obtained from ($\mathrm{SWD_{GNSS}}$) using the κ factor (in the same way as the conversion of $\mathrm{ZWD_{GNSS}}$ into $\mathrm{IWV_{GNSS}}$, as presented in Section 30.2.1.3):

$$\mathrm{SIWV_{GNSS}} = \kappa \ . \ \mathrm{SWD_{GNSS}} \tag{30.44}$$

30.3 Cases Studies of GNSS Meteorology

The most catastrophic meteorological situations, like cyclones, typhoons, hurricanes, or at a lower scale, huge storms, heavy rainfall, and flash-flood events, can unfortunately not be avoided. Loss of life, sadly, is frequent for such severe weather events, with heavy economic damage leading sometimes to social disasters. The only chance of saving lives and eventually property is to issue an official state of alert. This is the responsibility of emergency cells often managed by national meteorological institutions. Because the water vapor content of the troposphere is one of the key parameters during severe weather, naturally one comes to the conclusion that observations of the humidity field as part of the weather forecasting system are critical.

GNSS meteorology comprises three branches: GNSS radio occultation (RO), GNSS reflectrometry (GNSS-R), and GNSS ground-based measurements.

The GNSS RO technique is presented in Chapter 33. This technique has already shown promising prospects for monitoring tropical and extra-tropical cyclones [106], notably with the use of the global data set from FORMOSAT-3 (Formosa Satellite) and COSMIC-1 (Constellation Observing System for Meteorology, Ionosphere, and Climate) experiments.

Another important aspect of the monitoring of severe weather is the focus on hydrometeorology and land surface soil moisture. In fact, a study of the transfer of water and energy between the land surface and the lower atmosphere is essential in helping the emergency cells to judge the risk of flooding (after a cyclone, a typhoon, a large-scale storm, or a MCS). The GNSS-R technique for hydrology sensing is a promising tool (see Chapter 34). Some notable emerging meteorological applications include the monitoring of sea states at high risk, ocean eddy, and storm surges (see Chapter 34; [107]). The GNSS-R technique can use LEO satellite, airborne, or ground-based data. Note that the CYGNSS mission (Cyclone Global Navigation Satellite System) will use micro-satellites to measure wind speeds over Earth's oceans using reflected GPS signals, increasing scientists' ability to understand and predict hurricanes.

To elaborate on the interest in ground-based GNSS observations for the humidity field, this section focuses on two types of events (large-scale and mesoscale convection), provoking floods during autumn over southeastern France (also called "cévenol episode") and during the summer season in Belgium. These examples of the monitoring of severe weather situations use post-processed GNSS retrievals using GAMIT software (15 min time resolution for a cutoff angle of 10°). A description of other different kinds of events, like the West African monsoon and deep convection in the Amazon, is given by Bock et al. [99, 108], and Adams et al. [109].

30.3.1 Monitoring of Humidity Field from a Dense Network

In mid-August 2010, torrential rains over Belgium occurred. The origin of this heavy rain was a depression called "Yvette" by German meteorologists. A cold temperature anomaly in altitude created this low-pressure situation. At first, a high-altitude barometric hollow with a strong north-south component formed. Then the cold air moved toward the Southern regions, producing a low-pressure area topped with a dome of cold air. Yvette was

surrounded by high pressure almost everywhere (notably including the famous Russian anticyclone that was a source of great concern for Muscovites, who were struck at the same time by an unprecedented heat wave). Considering the slightly static comportment of the neighboring anticyclones, this depression became mature (with an occluded front) and literally emptied itself over Belgium. The location of Yvette brought quite surprising consequences in Europe: at the end of the afternoon of 15 August, the temperature was warmer in Finland (65°N) than in the Northwest of Spain (43°N), targeted by a North wind that followed the depression. This weather situation can be considered as a large-scale convective system, with a weather front passing slowly over Belgium. In 72 h, several Belgian rain gauge stations within a distance of a few hundred kilometers measured about 100 mm (or l/m^2) of accumulated rainfall, representing 150% of the mean monthly ratio. This rather rare phenomenon usually occurs in Belgium only every 20 years during the month of August.

Belgium is covered by a dense network of about 70 GNSS stations (baselines from 5 to 30 km; see Figure 30.7). This network is under the responsibility of the Flemish and Walloon government, the National Geographic Institute, and the Royal Observatory of Belgium (ROB). ZTD and gradients, running at the Royal Belgian Institute for Space Aeronomy (BIRA) using GAMIT software, have been retrieved with a time resolution of 15 min. Using ZTD combined with synoptic measurements of surface pressure and temperature, provided by the Royal Meteorological Institute of Belgium (RMI), images of the 2D field of IWV have been generated for the whole period of this rainfall event. Figure 30.7 shows the improvement in the monitoring of the humidity field following the strategy presented by Brenot et al. [82].

The motivation is to improve the horizontal distribution of the sites used to process interpolated IWV imaging. Considering the axis indicated by a gradient $\vec{G}$, two additional IWV pseudo-observations have been considered (one wetter in the direction of the vector and the other one drier in the opposite direction). Tests with the Belgian network have shown that 10 km on either side of the GNSS site is the most relevant distance for detecting small-scale structures of the troposphere (of a few kilometers). For each station, wet gradients (differential values in the zenith direction) have been converted into water vapor content gradients. To obtain pseudo-IWV, this kind of gradient can be propagated horizontally by multiplying its amplitude by the distance in kilometers [110]. Figure 30.8 presents a precise characterization of the water vapor field during this event.

From the 16th to the 17th of August 2010, precipitation occurred over the whole Belgian country, as shown by radar imaging Figure 30.8 (courtesy of Laurent Delobbe, RMI). Occasionally, it may happen that after a storm, a few isolated rain gauge stations record impressive accumulations. In the present case study, the entire country was affected. As well as this sudden heavy rainfall event, moderate rain took place continuously over more than 24 h in some areas. This situation is very unusual in summer for Belgium. IWV imaging of Figure 30.8 shows a contrast of dry and wet

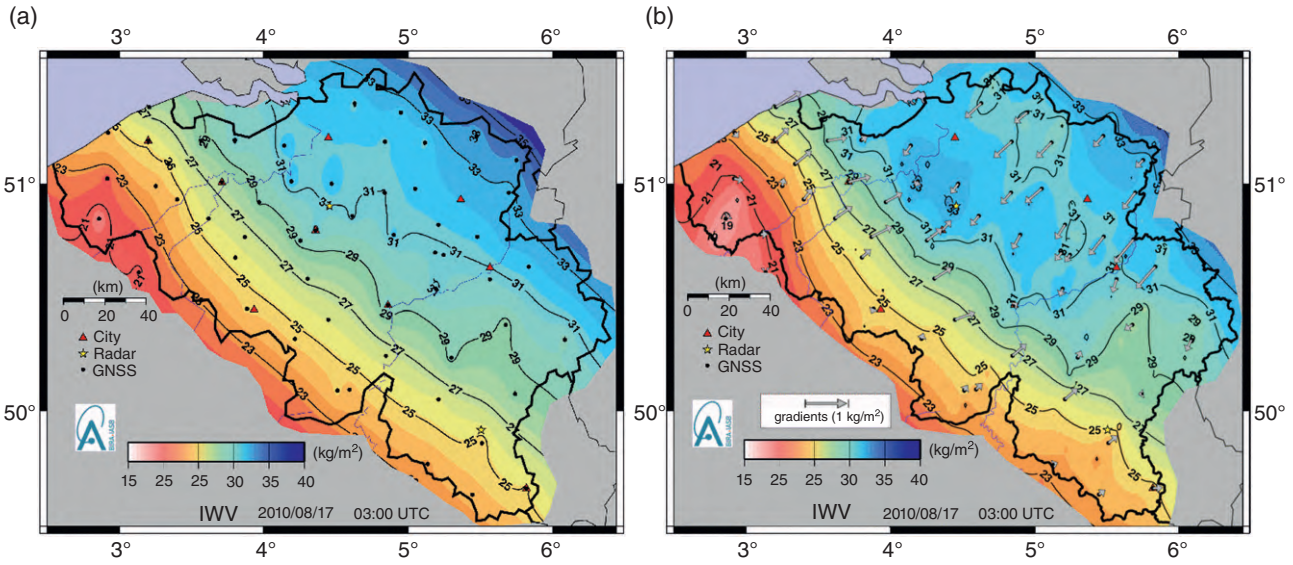

Figure 30.7 IWV imaging during the torrential rainfall of 15–17 August 2010 over Belgium: (a) classical interpolation, (b) integrating horizontal gradients.

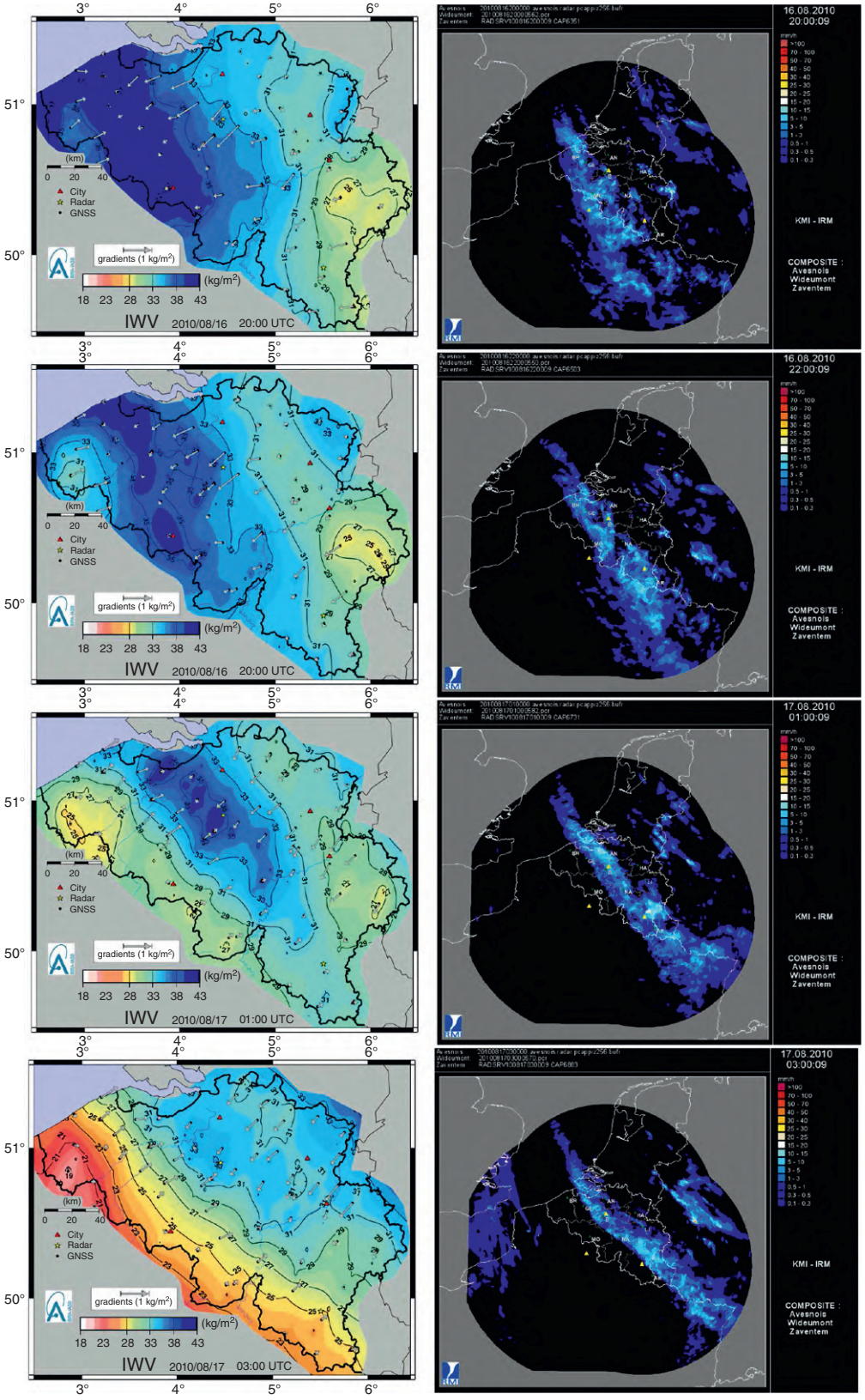

Figure 30.8 Imaging of IWV integrating horizontal gradients and composite radar precipitation in mm/h.

areas, basically in the northwest-southeast axis, which precisely describes the convergence line between the warm and cold fronts (seen at 01:00 UTC on 17 August 2010). The wet region corresponds exactly to the location of radar precipitation. The warm and dry area on the west side of Belgium is clearly identified. This weather front over Belgium is rigorously monitored by GNSS IWV imaging.

30.3.2 MCS and Retrievals of Local Anisotropy

Improving our knowledge of mesoscale phenomena [82, 111–113] is critical in warning the population in case of a high risk of flooding. The present case study contributes to the Cévennes-Vivarais Mediterranean Hydrometeorological Observatory (OHM-CV), which aims to understand and improve the forecast of frequent flash-flood events over the Cévennes-Vivarais region close to the Mediterranean coast in southeastern France [114]. The 8–9 September 2002 flash-flood event was characterized by an extreme precipitating convective situation, exhibiting both high hydrometeor content and non-hydrostatic effects due to convective upward and downward motions. A heavy precipitating system affected the Gard region. Twenty-four people were killed during this event, with the economic damage estimated at 1.2 billion euros [115].

Due to an upper cold low pressure centered over Ireland, extending to the Iberian Peninsula, a flow of air entered from the south during the night of 8–9 September. Associated with this upper level flow, a surface front undulated over western France. Convection formed ahead of the surface cold front, in the warm sector, where a moist low-level southeasterly flow prevailed. Triggered over the Mediterranean Sea during the early morning on 8 September 2002, the convective cells progressed northward to form inland after 08:00 UTC, a quasi-stationary MCS over the Gard region (see radar reflectivity/precipitation at 18:00 UTC, Figure 30.9). The quasi-stationary MCS remained over the same region until the following morning and then evolved eastward with the surface front. High surface rainfall was recorded over the Gard department, with a maximum recorded daily precipitation that reached about 700 mm in less than 24 h. A detailed description of this meteorological and hydrological event is presented by Delrieu et al. [114] and Chancibault et al. [116]. Three phases have been identified:

- In phase I (between 06:00 and 20:00 UTC on 8 September), the precipitation induced by the MCS was mainly over the plain region of the Gard department (Figure 30.9, at 18:00 UTC).
- Phase II (between 20:00 UTC on 8 September and 06:00 UTC on 9 September) was characterized by a shift of the MCS toward the upper regions at the limit of the mountain ridge (northeast of the CHRN station; Figure 30.9 at 23:00 UTC), where it merged with the surface front that had progressed eastward during the same period.
- In phase III (between 06:00 and 18:00 UTC on 9 September), the front with the embedded convection moved eastward and again swept over the Gard plain region.

Figure 30.10 shows a coupling of the ZTD-gradient time series from the 7th to the 10th of September 2002. With such a combined tool, the mean isotropic delay over the CHRN station (ZTD) and the mean anisotropic distribution of delay (gradients) can be presented using the same scale (with a mapping at 10°). Note that the delay variation is mainly driven by the water vapor, as presented in Section 30.2.1. The three phases identified are indicated in Figure 30.10.

Before phase I, gradients are almost nonexistent, with an isotropic delay L_{sym}^{10} being slightly stable. The mean delay at the CHRN station then increases significantly during phase I. At the beginning of this phase, gradients indicate

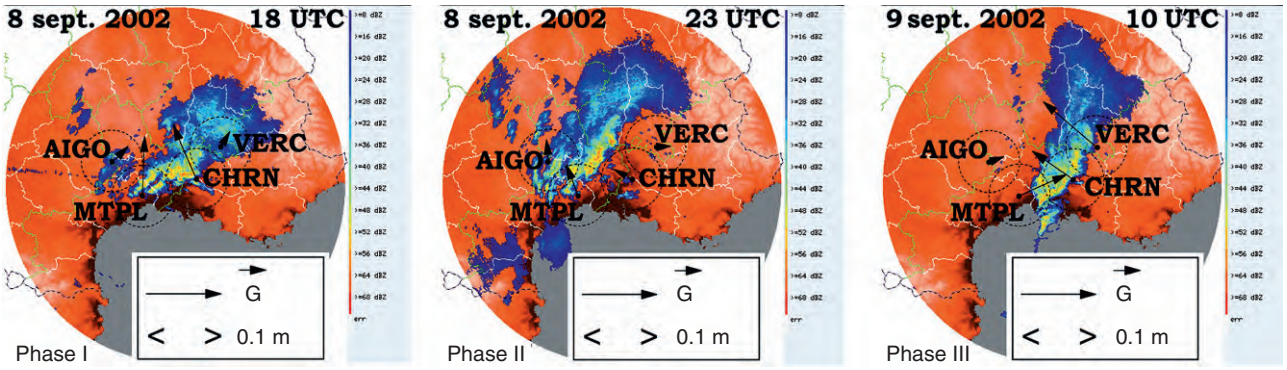

Figure 30.9 Reflectivity (in dBZ) of Bollène weather radar of Météo-France for the three phases of the flash-flood event of the Gard region (on 8–9 September 2002). Horizontal gradients $\vec{G}$ for four GNSS stations (CHRN, MTPL, AIGO, and VERC) are superimposed with circles in a dashed line showing their areas of representativity.

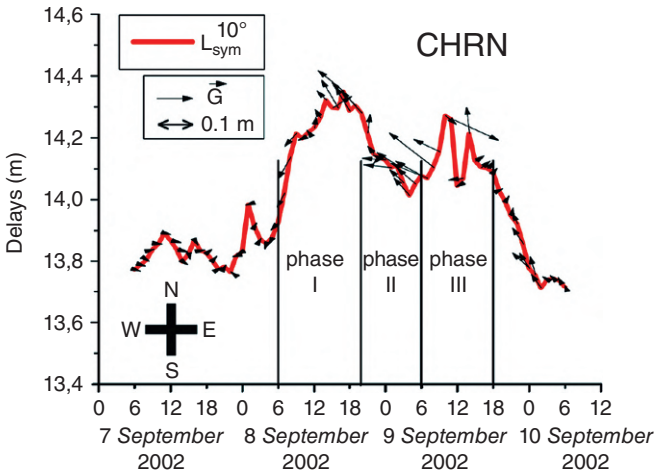

Figure 30.10 Coupling imaging of ZTD mapped at 10° of elevation (L_{sym}^{10}) combined with horizontal gradients $\left(\vec{G} = \begin{pmatrix} G_{NS} \\ G_{EW} \end{pmatrix}\right)$ also at 10° for CHRN station on 7–10 September 2002.

a flow of humidity on the southwestern side and finally point northwest of the CHRN station. This precisely describes the motion of the MCS during this phase, being initially over the Mediterranean Sea and finally on the northwestern side of CHRN. At the end of phase I, the mean isotropic delay reaches its maximum value when the MCS is the closest to the CHRN station. The same conclusion is observed for MTPL and VERC stations [41, 72]. At 18:00 UTC on 8 September, gradients of stations CHRN and MTPL clearly indicate the location of the MCS. Stations AIGO and VERC are inside the MCS and do not show any anisotropy with gradients.

During phase II, when the MCS moved northwest of CHRN, a consequent decrease of L_{sym}^{10}, is observed (Figure 30.10). At 23:00 UTC on 8 September, gradients from the CHRN and VERC stations are low, while MTPL gradient points in direction of the MCS (Figure 30.9). During this phase, the AIGO station, located on Mont Aigoual at an altitude of 1620 m, observes its maximum value for the mean isotropic delay (proximity to the MCS).

A mean increase of L_{sym}^{10} is observed at the CHRN station during phase III. The front passage and the embedded MCS over the Gard region is perfectly characterized by a peak at 10:00 UTC on 9 September. The gradients describe this passage exactly with a change of orientation north-west to south-east between 10:00 and 12:00 UTC. The MCS is perfectly highlighted by the three GNSS stations (MTPL, VERC, and CHRN), for which records of phase delays though the MCS have been observed (Figure 30.9). Note that the V-shape seen by radar reflectivity (at 10:00 UTC on 9 September) is typical for such a system with deep convection, especially in this French Gard area. Maximum convection acts at the edge of the V (highest vertical extension) and is associated with maximum precipitation. After phase III, the mean delay decreases to a slightly lower L_{sym}^{10} value than before phase I. Gradients again become almost nonexistent.

This cévenol episode has been studied in detail by Champollion et al. [72] and Brenot et al. [41], showing results from ZTD, gradients and residuals monitoring, and the validation of NWP experiments using GNSS measurements (the best simulation being the closest to GNSS observations). However, monitoring with slant delays in satellite directions has not been shown. Figure 30.11 presents STD skyplots with the tool presented in Figure 30.5 (Section 30.1.4.3). Using a selection of three STDs for each station during a defined period (phase II for AIGO, Figure 30.11a, and phase III for VERC, MTPL, and CHRN, Figure 30.11bcd), an effective scanning of the troposphere can proceed. Thanks to the geometry of the satellites (and with the assumption of a troposphere up to 10 km), the detection of fine-scale tropospheric structures (of 5–10 km) and heterogeneities (of 1–5 km) can be expected from this STD tool.

No structure or heterogeneity was observed at the AIGO station during phase I and III, but two structures and two heterogeneities are clearly detected in phase II (Figure 30.11a):

- On the west side at 23:30 UTC on 8 September 2002 (an elevation of about 40° for an azimuthal range of 15°), residuals detect a wet heterogeneity (maximum distance to Mont Aigoual of 9 km with a width of 2.5 km).
- Between 01:00 and 02:00 UTC on 9 September 2002, ZTD (i.e. L_{sym}) increases due to the proximity of the MCS (as shown on Figure 30.9 at 23:00 UTC on 8 September 2002). Gradients (via L_{az}) indicate a wet structure (MCS) on the east side of AIGO, and a finest-scale wet heterogeneity in the same direction is detected by STDs (via L_{res}; elevation of ~50°; azimuth range ~15°). The evaluation of the maximum distance to Aigoual is 8 km with a horizontal extension of about 2 km.

The VERC station did not record any structure during phases I and II. However, a structure and a heterogeneity are detected during phase III:

- Looking at Figure 30.11b, the passage of the MCS is seen at 11:00 UTC on 9 September 2002 (increase of L_{sym} in the southwest and northeast for an elevation of ~45° and ~70°, respectively). The gradients also clearly identify this structure between 09:00 and 10:00 UTC on the northwestern side of the VERC station. The size of the structure cannot be estimated. This MCS covered an area of about 80 × 40 km^2 at this time.
- On the southeastern of the VERC station, gradients indicate a dry structure at about 11:00 UTC on 9 September

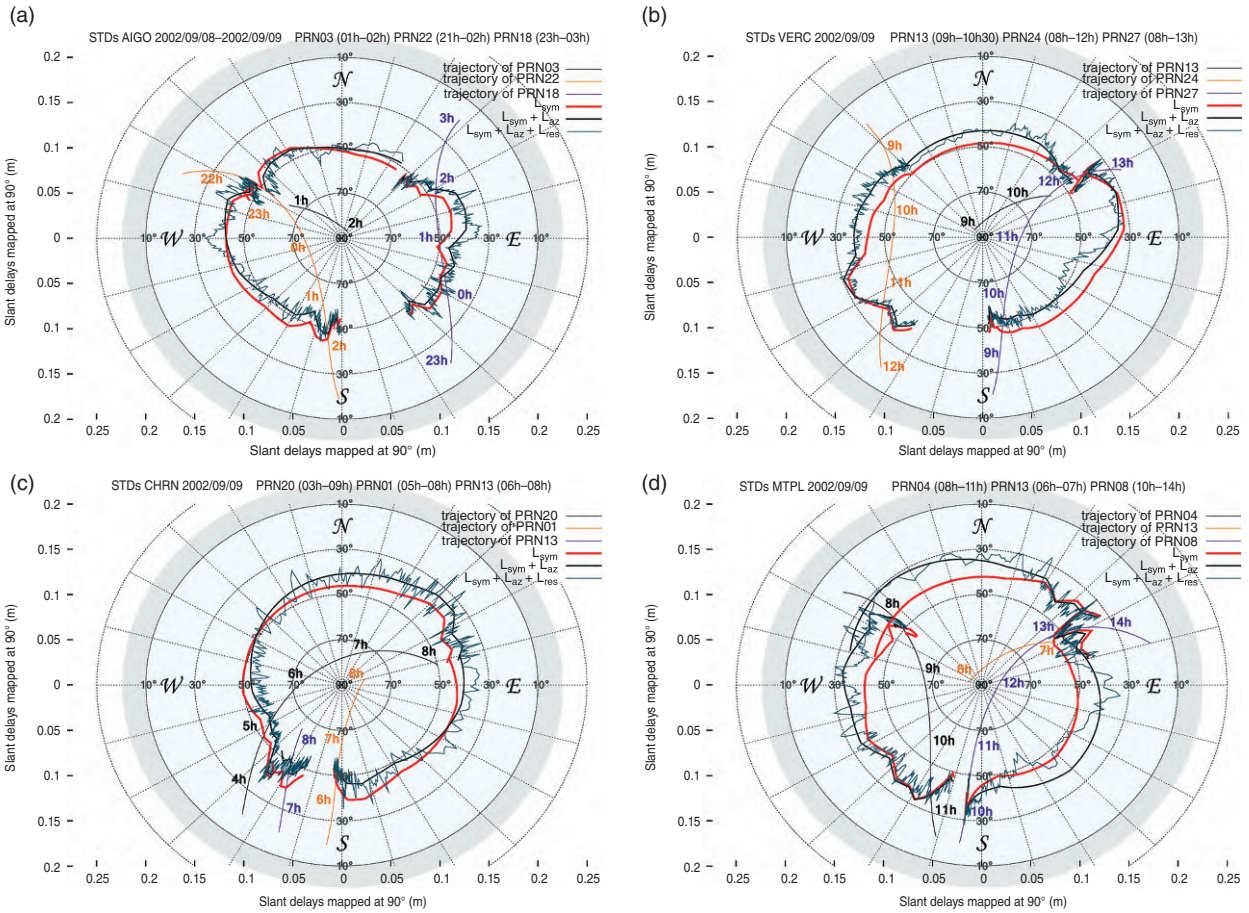

Figure 30.11 Contributions to slant delays (along the axes in black), in satellite directions (trajectories in brown, yellow, and purple lines; elevation in gray and azimuth described by cardinal points in black), mapped at 90° on 8–9 September 2002. The red lines show the isotropic contributions (L_{sym}); the black lines the additional anisotropic contributions () and the blue lines the STDs with residuals ($L_{sym} + L_{az} + L_{res}$). (a) A delay of 1.9 m has been subtracted from AIGO STDs, (b) 2.2 m to VERC STDs, (c) 2.4 m to MTPL, (d) 2.4 m to CHRN.

2002. A dry heterogeneity is observed by residuals (elevation of ~50°; azimuth range of ~25°). The evaluation of the maximum distance to VERC is 8.5 km, with a horizontal extension of about 3.5 km.

During the three identified phases, MTPL stations observed dry/wet structures and heterogeneities. A focus on phase III is presented in Figure 30.11c with the detection of a main structure with heterogeneities:

- The mean isotropic contribution from ZTD (L_{sym}) shows an increase between 07:00 and 08:00 UTC over MTPL on 9 September 2002. This corresponds to the passage of the MCS, as confirmed by the anisotropic contribution L_{az} from gradients (dry/wet contrast between STDs in the southwest and northeast directions).
- A panel of wet heterogeneities can be found north and east of MTPL, between 06:00 and 08:00 UTC. The horizontal extension of these heterogeneities does not exceed 2 km for a maximum distance of about 9 km.

Structures and heterogeneities are observed during phase I (see Figure 30.5) and phase III by the CHRN station. Figure 30.11d focuses on the last phase with structures and heterogeneities detected:

- Between 08:00 and 11:00 UTC on 9 September 2002, PRN04 observes a consequent increase of the isotropic contribution (peak of L_{sym}, as seen on Figure 30.10) for the passage of the MCS. Gradients (via L_{az} contribution) indicate a structure on the west and north sides of CHRN (from 06:00 to 09:00 UTC). The size of the structure cannot be determined. Many heterogeneities are detected by STDs without any clear identification.
- Between 13:00 and 14:00 UTC, PRN08 observes another consequent increase of the isotropic contribution (second peak of L_{sym}, Figure 30.10). The residuals detect a heterogeneity at 13:00 for the elevation of 50° but not for a lower elevation. The mean anisotropic contribution of gradients indicates that this structure is on the southeastern side of

CHRN, between 11:00 and 12:00 UTC. Finally, the last contribution of residuals to STDs (L_{res}) identifies a heterogeneity east of CHRN (elevation of ~80°; azimuth range of ~15°). The horizontal extension of these heterogeneities does not exceed 0.5 km for a maximum distance of about 1 km from the CHRN station.

Note that before and after the three identified phases, gradients and residuals are very low for the four stations ($L_{az} \approx L_{res} \approx 0$), and no heterogeneity is detected by STDs. The significant contribution of residuals to STDs (illustrated in skyplots in Figure 30.11) consolidates the study of Champollion et al. [72], showing the relevance of such an STD tool for forecasters.

30.3.3 Interest in GNSS Tomography for Nowcasting

The basic concept of GNSS tomography (for meteorology) is to use satellites as moving transmitters as well as a network of ground-based receivers to measure slant integrated measurements of the troposphere (i.e. STD, SWD, or SIWV; see Eqs. 30.19, 30.38, and 30.44). The objective is to retrieve respectively the three-dimensional field of the total atmospheric refractivity (N), the wet refractivity (N_{wet}) of the neutral atmosphere or the water vapor density (ρ_{wv}), as introduced by Flores et al. [80], Seko et al. [117], and Hirahara [118]. Comparisons of tomography retrievals with other techniques (WVR, radiosonde, Raman LiDAR, and atmospheric emitted radiance interferometer) and with numerical weather models have shown relevant results and an encouraging understanding of meteorological conditions [71, 81, 91, 119–133]. A good scenario for GNSS tomography is to adjust the three-dimensional fields of N, N_{wet}, and ρ_{wv} with a horizontal resolution of a few kilometers, a vertical resolution of 500 m in the lower troposphere (altitude between 0 and 5 km) and 1 km in the upper troposphere (altitude from 5 to about 12 km, depending on the tropopause), and a time resolution of 5 to 15 min. A dense homogeneously distributed network of GNSS stations (e.g. 5–25 km spacing) is required. Using the Belgian dense network introduced in Section 30.3.1, GNSS tomographic retrievals of ρ_{wv} (with a time resolution of 5 min) have been computed to study the storm of 18 August 2011 over Belgium. An overview of the situation is presented in the next paragraph.

As expected by meteorological models, for example, from ALARO model from RMI, a thermal depression reached Belgium late in the afternoon (18 August 2011). It was accompanied by warm and wet air masses, especially in the lowest layers of the atmosphere, while the top layers were rather cold, producing an unstable system. High values of convective available potential energy (CAPE) and jet stream at high altitude favored windshear, forming an explosive cocktail. This kind of thunderstorm can cause a strong downburst that can inflict damage comparable to the passage of a small tornado. Most of Belgium was affected by violent thunderstorms. These were accompanied locally by intense rain, hail, and gusts of wind, which caused a flood event in Brussels and blocked 300 km of road traffic. At this time, forecasters could not precisely describe the meteorological situation and anticipate its dramatic consequences. Pouring rain, destructive gusts of wind up to more than 110 km/h, and hail caused damage in Belgium.

Continuing its progress northeast of Brussels, the thunderstorm reached Hasselt in the Limburg region. The combined effect of violent winds and the weight of precipitation on the covers caused a stage of the Pukkelpop festival to collapse (end of the afternoon), hurting 40 people (6 seriously) and causing five deaths.

Since the tragedy, the use of GNSS tomography for monitoring this event has been investigated. The grid retrieved is $20 \times 20 \times 0.5$ km. Outputs from the ALARO model (4 km resolution) have been used to define the a priori condition of the tomography.

With a similar approach to the one presented in Section 30.3.1, pseudo-IWV observations have been implemented and mapped in satellite directions (using mf^{w}_{sym} mentioned Section 30.1.4.1):

$$\text{pseudo} - \text{SIWV}(\epsilon_i) = \text{pseudo} - \text{IWV} \ . \ mf^{w}_{sym}(\epsilon_i) \tag{30.45}$$

To validate this new approach in GNSS tomography, IWVs have been back-calculated using tomographic ρ_{wv} retrievals (IWV_{tomo}) and then compared with IWV_{GNSS}. The mean bias between IWVs estimated from the a priori condition used in tomography ($\text{IWV}_{apriori}$) with IWV_{GNSS} has also been studied.

Table 30.1 shows the results of comparisons according to two choices of a priori condition for the tomography (standard atmosphere of 1976 and ALARO outputs) with mean IWV biases of −12.4 and 3.6 kg/m^2, respectively. Using a classical strategy, the best a priori condition (the one from ALARO) gives the lowest bias with IWV_{GNSS} (mean biases from −9.7 to 3.2 kg/m^2). The new strategy with pseudo-IWV increases the number of voxels adjusted by 15%, and decreases the mean IWV bias by 0.9 kg/m^2.

Figures 30.13 and 30.14 show ρ_{wv} from ALARO NWP (courtesy of Alex Deckmyn, RMI) and tomographic retrievals at 15:35 UTC (18 August 2011); the time shown here is a few hours before the dramatic event at the Pukkelpop festival (latitude 50.96°N, longitude 5.36°E). To improve the geometrical representativity of the tomographic inversion, pseudo-SIWV observations have been used (see Figure 30.12), showing

Table 30.1 Comparison of mean bias of IWV to validate a new strategy in GNSS tomography

A priori condition used	Tomography strategy	Voxels adjusted (in %)	Mean bias (kg/m^2) $IWV_{apriori} - IWV_{GNSS}$	Mean bias (kg/m^2) $IWV_{tomo} - IWV_{GNSS}$
Standard atmosphere	Classical	61.5	−12.4	−9.7
ALARO	Classical	61.5	3.6	3.2
ALARO	Pseudo-SIWV	76.5	3.6	2.3

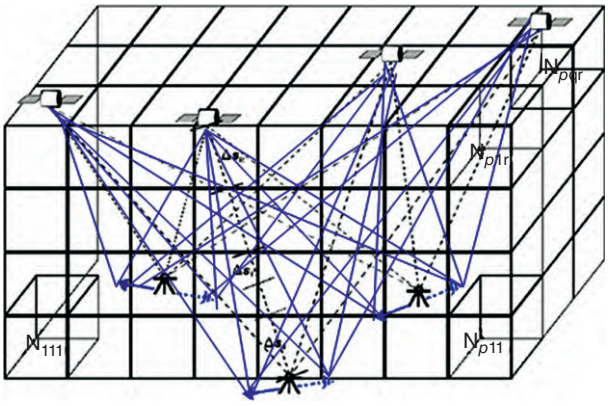

Figure 30.12 Illustration of the improvement of the geometrical distribution of slant observations used in GNSS tomography. Additional pseudo-SIWV (blue lines), as defined by horizontal gradients (in blue), are considered.

good results. Significant differences between ALARO and tomographic retrievals can be observed. For altitudes between 0.25 and 3.25 km, GNSS shows higher ρ_{wv} values than ALARO on the northeastern side of Belgium (location of Hasselt and the Pukkelpop festival) and the lowest values on the northwestern side. With a relevant description of the 3D field of water vapor (particularly for the lower layer of the troposphere), GNSS tomography can improve our understanding of this event and help forecasters in their task. The capability of the GNSS technique to detect three-dimensional wet/dry structures of the troposphere is of real interest for nowcasting.

30.4 Present and Future Applications in Synergy with Other Techniques

This study presents the meteorological interest in using GNSS zenith delays, horizontal gradients, residuals, and slant delays of the neutral atmosphere for monitoring severe weather events (e.g. a flash flood in southeastern France in September 2002, and heavy rainfall events in Belgium during August 2010 and 2011). The high time resolution of these measurements (e.g. 5 to 15 min for zenith delays and gradients, and 30 s for slant delays and residuals) retrieved with high variation (low constraints for ZTD and gradients) is required for atmospheric monitoring. Using a dense network of stations (ideally with a mean baseline of 5 to 25 km), severe weather situations can be closely monitored by GNSS two-dimensional fields of total delay, wet delay, and humidity. Relevant improvement of the horizontal resolution of these fields can be obtained using pseudo-observations estimated from gradients. GNSS tropospheric retrievals have been initially validated using measurements from other instruments, such as radiosonde or microwave radiometer; however, at the present time, and thanks to its stability, ZTD_{GNSS}, ZWD_{GNSS} or IWV_{GNSS} can be used as a reference for developing observations from other instruments (e.g. validation of sensors on board polar orbiting satellites, for retrieving total column of water vapor). The studies presented in this chapter focus only on GPS data; however, incorporating multi-GNSS will bring benefits for troposphere monitoring and other GNSS applications more generally. Bender et al. [134] illustrate the interest of multi-GNSS (i.e GPS, GLONASS, and Galileo) for improving tomography retrievals (increase of the spatio-temporal resolution of the reconstructed humidity fields and of its quality). Ding et al. [135] evaluate real-time troposphere estimation, showing that incorporating observations from multi-GNSS inside a PPP analysis system can increase the performance of real-time ZTD retrievals, especially for weather nowcasting. Guerova et al. [136] present the state of the art and future prospects of ground-based GNSS meteorology in Europe. This study contributes to the COST Action ES1206 (called GNSS4SWEC), notably bringing a focus on the three axes of this European common effort (i.e. on advanced GNSS processing for near-real-time applications, the assimilation of GNSS tropospheric products in NWP models, and GNSS for climate monitoring). A presentation of the benchmark campaign used by the GNSS4SWEC community can be found in Douša et al. (2016).

A short summary of present applications for tropospheric water vapor estimates from ground-based GNSS data is as follows:

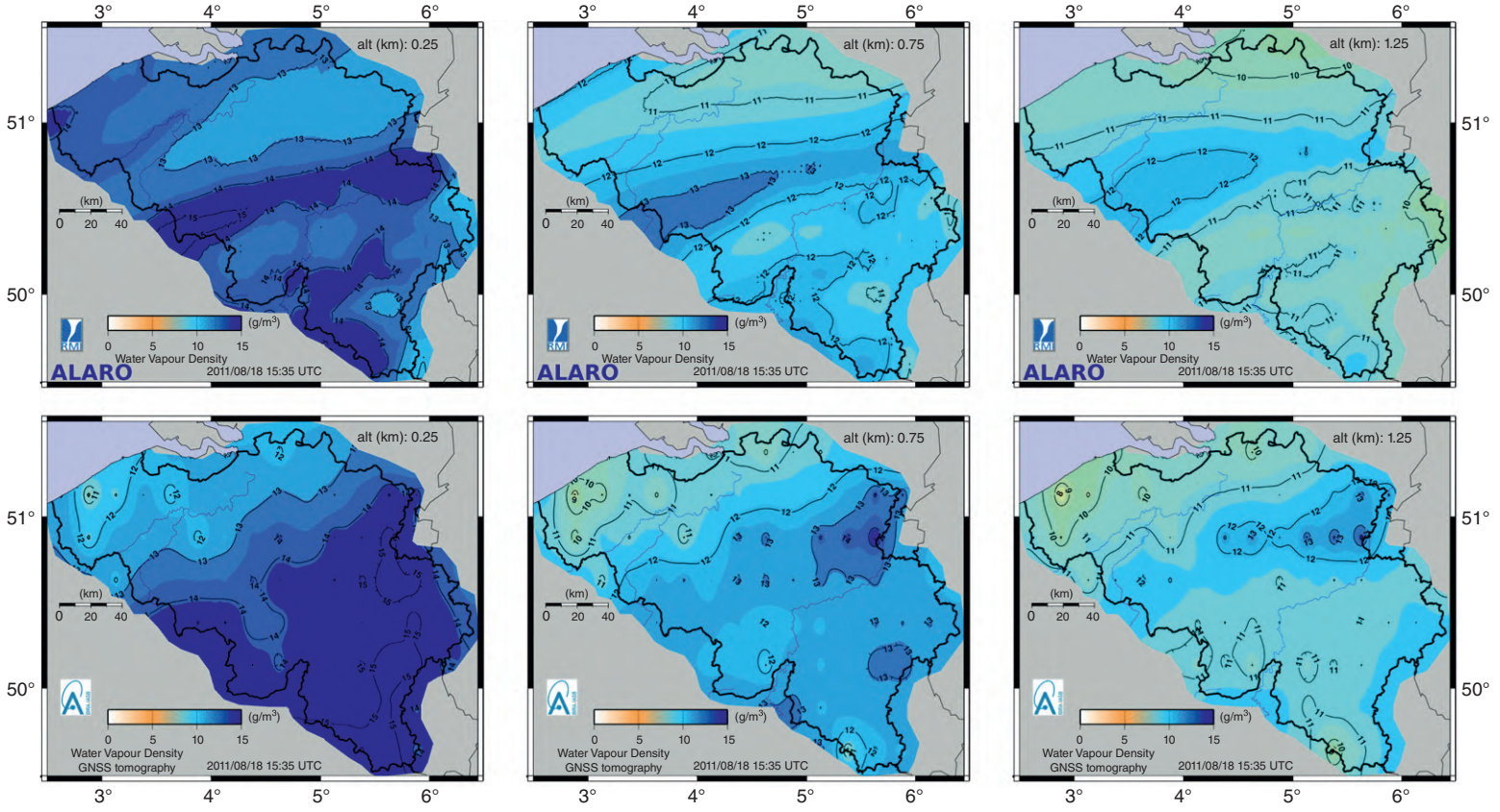

Figure 30.13 ALARO outputs and tomographic retrievals (altitude of 0.25 km, 0.75 km, and 1.25 km).

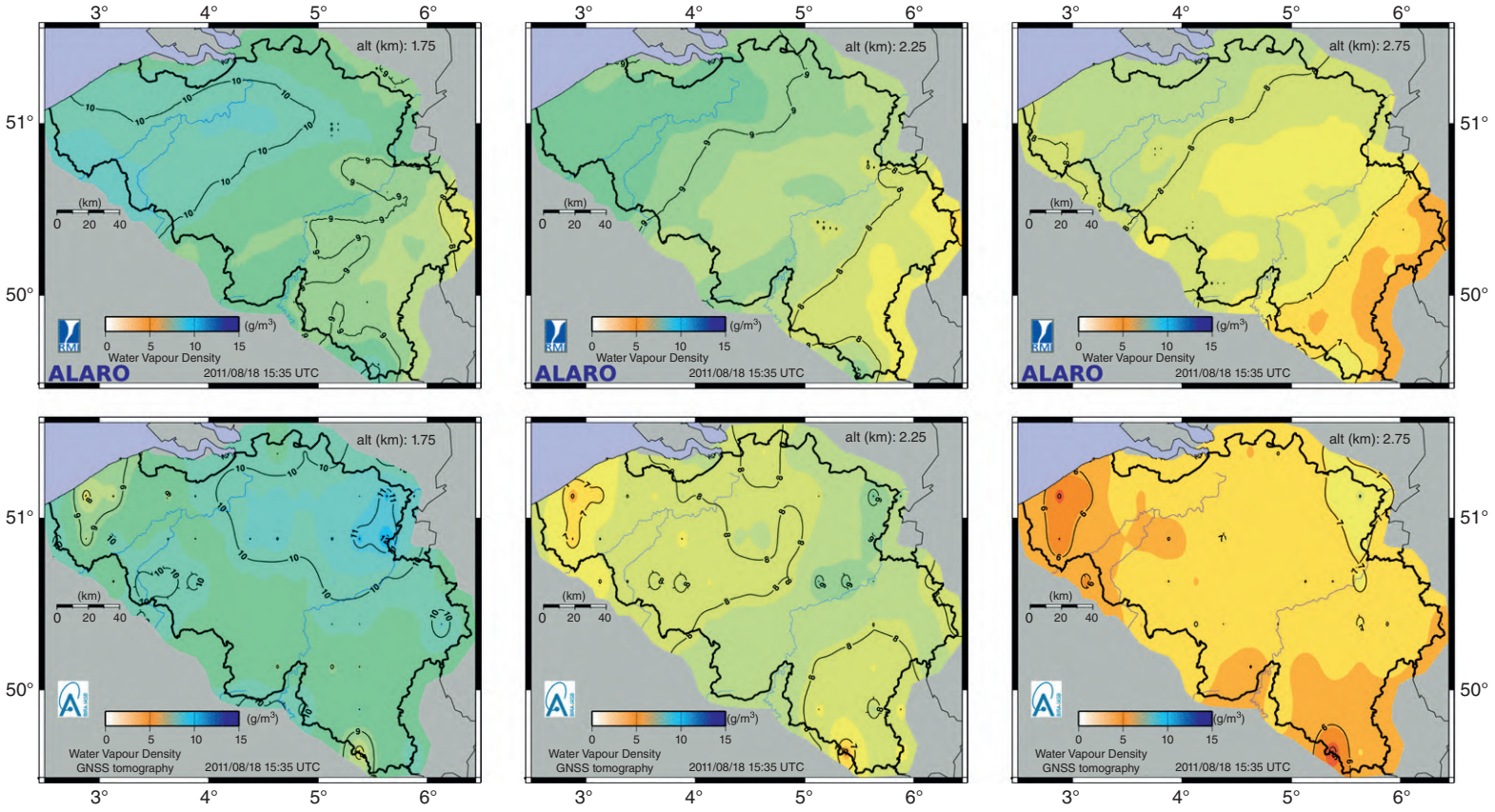

Figure 30.14 ALARO outputs and tomographic retrievals (altitude of 1.75 km, 2.25 km, and 2.75 km).

- Study of meteorological events from post-processed GNSS retrievals (ZTD, gradients, residuals, IWV, STD, and SIWV) and tomography retrievals of wet refractivity and water vapor density.
- Validation of NWP using GNSS observations.
- Real-time GNSS monitoring (ZTD, ZWD, and IWV).
- The assimilation of ZTD/STD in operational NWP systems.
- Climatological applications by post-processing long time series of data with the same coherent analysis strategy (homogenization).

A lot of work is currently underway in the GNSS meteorology community. Here is a brief sample of ongoing applications and future synergies that use ground-based GNSS tropospheric estimates:

- Validation of GNSS slant delays various different software (continuation of the work of Braun et al. [137]; see [138])
- Validation of water vapor observations from other instruments (e.g. sensors onboard satellite platforms).
- Improvement of GNSS tomography in regions with strong topography, and use of a geometrical matrix describing a more realistic propagation through the neutral atmosphere (see ray tracing from [139, 140]).
- Combined tomographic retrievals between ground-based GNSS with other techniques (e.g. with GNSS RO, nadir and limb measurements from IR and UV sensors, and other ground-based instruments, e.g. microwave radiometers, LiDAR, sun photometers, or spectrometers).
- The use of new GNSS products by forecasters (e.g. as an indicator of deep convection, near-real-time tomography, perturbations of signals, and implementations of indexes of atmospheric activity).
- Atmospheric perturbations of GNSS signals and their impact on real-time kinematic (RTK) positioning (see Chapter 19).
- Disruptions of GNSS signals and implementations of atmospheric media calibration for deep space network.
- Attenuation and delay of GNSS signals by volcanic ash [141–144].
- Synergy of a synthetic aperture radar with GNSS tomography [145].
- Flagging of hydrometeor delays in GNSS signals and synergy between weather radar and GNSS monitoring.

These examples of present and future contributions represent only a small sample of the progress of the research in this field. Based on these remarkable results already established by GNSS (from precise positioning to meteorological observations), it is reasonable to hope that there will be further discoveries and advances in the field of atmospheric monitoring, especially with synergy between the three branches (radio occultation, reflectometry, and the ground-based GNSS technique).

References

1 Spilker, J. (1978) *Global Positioning System*, *Journal of The Institute of Navigation*, Washington, DC., chap. GPS Signal Structure and Performance Characteristics, pp. 29–54.

2 Langley, R.B. (1990). Why is GPS signal so complex? *GPS World* 1 (3): 56–59.

3 Klobuchar, J.A. (1983). *Ionospheric effects on earth-space propagation, AFGL-TR-84-0004*. Air Force Laboratory.

4 Rummel, R. and Rapp, R.H. (1976). The influence of the atmosphere on geoid and potential coefficient determinations from gravity data. *J. Geophys. Res.* 81: 5639–5642.

5 Black, H.D. (1978). An easy implemented algorithm for the tropospheric range correction. *J. Geophys. Res.* 83: 1825–1828.

6 Thomas, J.B., Fanselow, J.L., MacDoran, P.F. et al. (1976). A Demonstration of an independent-station radio interferometry system with 4-cm precision on 16-km base line. *J. Geophys. Res.* 81: 995–1005.

7 Rogers, A.E.E., Knight, C.A., Hinteregger, H.F. et al. (1978). Geodesy by radio interferometry: Determination of a 1.24-km base line vector with ≈ 5-mm repeatability. *J. Geophys. Res.* 83: 325–334.

8 Cannon, W.H., Langley, R.B., Petrachenko, W.T., and Kouba, J. (1979). Geodesy and astrometry by transatlantic long base line interferometry. *J. Geophys. Res.* 84: 229–236.

9 Herring, T.A., Corey, B.E., III, C.C.C., Shapiro, I.I., Rönnäng, B.O., Rydberg, O.E.H., Clark, T.A., Coates, R.J., ma, C., Ryan, J.W., Vandenberg, N.R., Hinteregger, H.F., Knight, C.A., Rogers, A.E.E., Whitney, A.R., Robertson, D.S., and Schupler, B.R. (1981) Geodesy by radio interferometry: Intercontinental distance determinations with subdecimeter precision. *J. Geophys. Res.*, 81, 1647–1651.

10 Hopfield, H.S. (1969). Two-quartic tropospheric refractivity profile for correcting satellite data. *J. Geophys. Res.* 74: 4487–4499.

11 Marini, J.W. (1972). Correction of satellite tracking data for arbitrary atmospheric profile. *Radio Science* 7: 223–231.

12 Davis, J.L., Herring, T.A., Shapiro, I.I. et al. (1985). Geodesy by interferometry: Effects of atmospheric modeling errors on estimates of baseline length. *Radio Science* 20: 1593–1607.

13 Herring, T.A. (1986). Precision of vertical position estimates from very long baseline interferometry. *J. Geophys. Res.* 91: 9177–9182.

14 Kroger, P.M., Davidson, J.M., and Gardner, E.C. (1986). Mobile very long baseline interferometry and Global Positioning System measurement of vertical crustal motion. *J. Geophys. Res.* 91: 9169–9176.

15 Ware, R.H. and Hurst, C.R.K.J. (1986). A Global Positioning System baseline determination including bias fixing and water vapor radiometer corrections. *J. Geophys. Res.* 91: 9183–9192.

16 Bossler, J.D., Goad, C.C., and Bender, P.L. (1980). Using the Global Positioning System (GPS) for geodetic surveying. *Bulletin Géodésique* 54: 553–563.

17 Bender, P.L. and Larden, D.R. (1985). *GPS carrier phase ambiguity resolution over long baselines, in the First International Symposium on Precise Positioning with GPS*. Rockville, MD: NOAA.

18 Bock, Y.R., Abbot, R.I., III, C.C.C., Gourevitch, S.A., and King, R.W. (1985) Establishment of three-dimensional geodetic control via interferometry with Global Positioning System. *J. Geophys. Res.*, 90, 7689–7703.

19 Tralli, D.M., Dixon, T.H., and Stephens, S.A. (1988). Effect of wet troposheric path delays on estimations of geodetic baselines in the Gulf of California using Global Positioning System. *J. Geophys. Res.* 93: 6545–6557.

20 Lichten, S.M. and Border, J.S. (1987). Strategies for high-precision Global Positioning System orbit determination. *J. Geophys. Res.* 92 (B12): 12 751–12 762.

21 King, R.W., Masters, E.G., Rizos, C. et al. (1985). *Surveying with GPS, Monograph 9*. School of Surveying: University of New South Wales, Kensington, Australia.

22 Dong, D.N. and Bock, Y. (1989). Global Positioning System network analysis with phase ambiguity resolution applied to crustal deformation studies in California. *J. Geophys. Res.* 94: 3949–3966.

23 Blewitt, G. (1989). Carrier phase ambiguity resolution for the Global Positioning System applied to geodetic baselines up to 2000 km. *J. Geophys. Res.* 94: 10,187–10,203.

24 Leick, A. (1989). *GPS Satellite Surveying*. Wiley-Interscience.

25 Teunissen, P., Kleusberg, A., Bock, Y. et al. (1998). *GPS for Geodesy*, 2nde. Springer.

26 Tralli, D.M. and Lichten, S.M. (1990). Stochastic estimation of tropospheric path delays in Global Positioning System geodetic measurements. *Bull. Géod.* 64: 127–159.

27 Gurtner, W. (1994). RINEX: The receiver-independent exchange format. *GPS World* 5: 48–52.

28 Bevis, M., Businger, S., Herring, T.A. et al. (1992). GPS Meteorology: Remote sensing of atmospheric water vapor using the Global Positioning System. *J. Geophys. Res.* 97 (D14): 15 787–15 801.

29 Hogg, D.C., Guiraud, F.O., and Decker, M.T. (1981). Measurement of excess transmission length on Earth-Space paths. *Astron. Astrophys.* 95: 304–307.

30 Askne, J. and Nordius, H. (1987). Estimation of tropospheric delay for microwaves from surface weather data. *Radio Science* 22 (3): 379–386.

31 Businger, S., Chiswell, S., Bevis, M. et al. (1996). The promise of GPS in atmospheric monitoring. *Bull. Amer. Meteorol. Soc.* 77 (1): 5–18.

32 Duan, J., Bevis, M., Fang, P. et al. (1996). GPS Meteorology: Direct estimation of the absolute value of precipitable water. *J. Appl. Meteor.* 35: 830–838.

33 Rocken, C., Ware, R., Hove, T.V. et al. (1993). Sensing atmospheric water vapor with the Global Positioning System. *Geophys. Res. Lett.* 20: 2631–2634.

34 Rocken, C., Hove, T.V., Johnson, J. et al. (1995). GPS/STORM: GPS sensing of atmospheric water vapor for meteorology. *J. Atmos. Ocean. Tech.* 12: 2631–2634.

35 Tregoning, P., Boers, R., O'Brien, D., and Hendy, M. (1998). Accuracy of absolute precipitable water vapor estimates from GPS observations. *J. Geophys. Res.* 103 (D22): 28,701–28,710.

36 Niell, A., Coster, A., Solheim, F. et al. (2001). Comparison of measurements of atmospheric wet delay by radiosonde, water vapor radiometer, GPS, and VLBI. *J. Atmos. Oceanic Technol.* 18: 830–850.

37 Saastamoinen, J. (1972) Atmospheric Correction for the Troposphere and Stratosphere in Radio ranging of satellites. *Geophys. Monogr. Ser.*, 15 (eds. S.W. Henriksen et al.), pp. 247–251.

38 Kursinski, E., Hajj, G., Schofield, J. et al. (1997). Observing Earth's atmosphere with radio occultation measurements using the Global Positioning System. *J. Geophys. Res.* 102 (D19): 23,429–23,465.

39 Solheim, F., Vivekanandan, J., Ware, R., and Rocken, C. (1999). Propagation delays induced in GPS signals by dry air, water vapor, hydrometeors, and other particulates. *J. Geophys. Res.* 104 (D4): 9663–9670.

40 Hajj, G., Kursinski, E., Romans, L. et al. (2002). A technical description of atmospheric sounding by GPS occultation. *J. Atmos. Solar-Terres. Phys.* 64: 451–469.

41 Brenot, H., Ducrocq, V., Walpersdorf, A. et al. (2006). GPS Zenith delay sensitivity evaluated from high-resolution NWP simulations of the 8–9th September 2002 flash-flood over southeastern France. *J. Geophys. Res.* 111: D15105. https://doi.org/10.1029/2004JD005726.

42 Resch, G.M. (1984). *Geodetic Refraction*, Springer-Verlag, New York, chap. *Water vapor radiometry in geodetic applications, pp.*: 53–84.

43 Yionoulis, S.M. (1970). Algorithm to compute tropospheric refraction effects on range measurements. *J. Geophys. Res.* 75: 7636–7637.

44 Chao, C.C. (1972). *A Model for Tropospheric Calibration from Daily Surface and Radiosonde Balloon Measurements, Technical Memorandum 391-350*. Pasadena, California: JPL.

45 Marini, J.W. and Murray, C.W. (1973). *Correction for Laser Range Tracking Data for Atmospheric Refraction at*

Elevation above 10 Degrees, Report X-591-73-351. Greenbelt, MD: NASA GSFC.

46 Moffett, J.B. (1973) Program Requirements for Two-Minute Integrated Doppler Satellite Navigation Solution, Technical Memorandum TG 819-1, Applied Physics Laboratory, The Hopkins University, Laurel, MD.

47 Saastamoinen, J. (1973). Contribution to the theory of atmospheric refraction (1^{ere} partie). *Bulletin Géodésique* 105: 279–298.

48 Saastamoinen, J. (1973). Contribution to the theory of atmospheric refraction (2^{eme} partie): Introduction to practical computation of astronomical refraction. *Bulletin Géodésique* 106: 383–397.

49 Saastamoinen, J. (1973). Contribution to the theory of atmospheric refraction (3^{eme} partie). *Bulletin Géodésique* 107: 13–34.

50 Goad, C.C. and Goodman, L. (1974) A modified Hopfield tropospheric correction model, *Presented at the American Geophysical Union Fall Annual Meeting*, San Francisco, California, 12–17 December, 28 pp.

51 Black, H.D. and Eisner, A. (1984). Correcting satellite doppler data for tropospheric effects. *J. Geophys. Res.* 89: 2616–2626.

52 Lanyi, G.E. (1984). *Troposheric Delay Affecting Radio Interferometry, TDA Progress Report 42-78*. Pasadena: JPL.

53 Ifadis, I.I. (1986). *The Atmospheric Delay of Radio Wave: Modelling the Elevation the Elevation Dependence on a Global Scale, Technical Report #38L*. Göteborg, Sweden: Chalmers University of Technology.

54 Santerre, R. (1987). *Tropospheric refraction effects in GPS positioning, SE 6910 Graduate Seminar Department of Surveying Engineering*. Fredericton, Canada: University of New Brunswick.

55 Baby, H.B. and Labergnat, P.G.J. (1988). A model for the tropospheric excess path length of radio waves from surface meteorological measurements. *Radio Science* 23: 1023–1038.

56 Rahnmoon, M. (1988) Ein neues Korrekturmodell fr Mikrowellen – Entfernungsmessungen zu Satelliten, PhD thesis, Munich, F. R. G., [en allemand].

57 Herring, T.A. (1992) Modeling atmospheric delays in te analysis of space geodetic data, *Proceedings of the Symposium on Refraction of Transatmospheric Signals in Geodesy,* Netherlands Geodetic Commission, Publications on Geodesy, Delft, the Netherlands

58 Niell, A. (1996). Global mapping functions for the atmosphere delay at radio wavelengths. *J. Geophys. Res.* 101: 3227–3246.

59 Boehm, J., Werl, B., and Schuh, H. (2006a). Troposphere mapping functions for GPS and very long baseline interferometry from European Centre for Medium-Range Weather Forecasts operational analysis data. *J. Geophys. Res.* 111 (B02): 406. https://doi.org/10.1029/2005JB003 629.

60 Boehm, J., Niell, A.E., Tregoning, P., and Schuh, H. (2006b). Global mapping function (GMF): A new empirical mapping function based on numerical weather model data. *Geophys. Res. Lett.* 33 (L07): 304. https://doi.org/10.1029/2005GL025 546.

61 Spilker, J.J. (1980) *Global Positioning System*, Vol. I., The Institute of Navigation.

62 Brunner, F.K. and Gu, M. (1991). An improved model for the dual frequency ionospheric correction of GPS observations. *Manuscr. Geod.* 16: 205–214.

63 Zumberge, J.F., Heflin, M.B., Jefferson, D.C. et al. (1997). Precise point positioning for the efficient and robust analysis of GPS data from large networks. *J. Geophys. Res.* 102: B3. https://doi.org/10.1029/96JB03860.

64 Herring, T.A., King, R.W., Floyd, M.A., and McClusky, S.C. (2015) Documentation for the GAMIT GPS Analysis Software, version 10.16, *Tech. Rep*., Mass. Inst. Tech., Cambridge. Http://www.gpsg.mit.edu/simon/gtgk/docs.htm.

65 Blewitt, G. (1998) *GPS for Geodesy*, 2nd Ed., chap. 6, pp. 231–270, Springer.

66 Davis, J.L., Elgered, G., Niell, A.E., and Kuehn, C.E. (1993). Groundbased measurements of gradients in the "wet" radio refractivity of air. *Radio Science* 28: 1003–1018.

67 MacMillan, D.S. (1995). Atmospheric gradients from very long baseline interferometry observations. *Geophys. Res. Lett.* 22 (9): 97–102. https://doi.org/10.1029/95GL00887.

68 Alber, C., Ware, R.H., Rocken, C., and Solheim, F.S. (1997). GPS surveying with 1 mm precision using corrections for atmospheric slant path delays. *Geophys. Res. Lett.* 24: 1859–1862.

69 Chen, G. and Herring, T.A. (1997). Effects of atmospheric azimuthal asymmetry on the analysis of space geodetic data. *Geophys. Res. Lett.* 102: 20489–20502.

70 Bar-Sever, Y.E. and Kroger, P.M. (1998). Estimating horizontal gradients of tropospheric path delay with a single GPS receiver. *J. Geophys. Res.* 103: 5019–5035.

71 Gradinarsky, L.P. (2002) Sensing Atmospheric Water Vapor Using Radio Waves, Ph.D. thesis, School of Electrical Engineering, Chalmers University of Technology, Göteborg, Sweden.

72 Champollion, C., Masson, F., Van Baelen, J. et al. (2004). GPS monitoring of the tropospheric water vapour distribution and variation during the September 9, 2002,Torrential Precipitation Episode in the Cévennes (Southern France). *J. Geophys. Res.* 109: D24.

73 Pany, T., Pesec, P., and Stangl, G. (2001). Elimination of tropospheric path delays in GPS observations with the

ECMWF numerical weather model. *Phys. Chem. Earth* 26: 487–492.

74 Elósegui, P., Davis, J.L., Jaldehag, R.T.K. et al. (1995). Geodesy using the Global Positioning System: The effects of signal scattering on estimates of site position. *J. Geophys. Res.* 100: 9921–9934.

75 Iwabuchi, T., Shoji, Y., Shimada, S., and Nakamura, H. (2004). Tsukuba GPS dense net campaign observations: Comparison of the stacking maps of post-fit phase residuals estimated from three software packages. *J. Met. Soc. Japan* 82 (1B): 315–330.

76 Shoji, Y., Nakamura, H., Iwabuchi, T. et al. (2004). Tsukuba GPS dense net campaign observation: Improvement in GPS analysis of slant path delay by stacking one-way postfit phase residuals. *J. Met. Soc. Japan* 82 (1B): 301–314.

77 Schupler, B.R. and Clark, T.A. (November/December, 1991) How different antennas affect the GPS observable. *GPS World.*

78 Rothacher, M. and Mader, G. (1996). *Combination of antenna phase center offsets and variations, Antenna Calibration Set IGS_01*. IGS Central Bureau: University of Berne, Switzerland.

79 Schupler, B.R. (2001). The response of GPS antennas – how design, environment and frequency affect what you see. *Phys. Chem. Earth* 26: 605–611.

80 Flores, A., Ruffini, G., and Ruis, A. (2000). 4D Tropospheric Tomography Using GPS Slant Wet Delays. *Ann. Geophys.* 18: 223–234.

81 Brenot, H., Walpersdorf, A., Reverdy, M., Van Baelen, J., Ducrocq V., Champollion, C., Masson, F., Doerflinger, E., Collard, P., and Giroux, P. (2014) A GPS network for tropospheric tomography in the framework of the Mediterranean hydrometeorological observatory Cévennes-Vivarais (southeastern France). *Atmos. Meas. Tech.*, 7, doi.org/10.5194/amt-7-553-2014, 553–578.

82 Brenot, H., Neméghaire, J., Delobbe, L., Clerbaux, N., Ducrocq V., De Meutter, P., Deckmyn, A., Delcloo, A., Frappez, L., and Van Roozendael, M. (2013) Preliminary signs of the initiation of deep convection by GNSS. *Atmos. Chem. Phys.*, 13, doi.org/10.5194/acp-13-5425-2013, 5425–5449.

83 Kämfer, N. (2013) Monitoring Atmospheric Water Vapour, ISSI Scientific Report Series, 10, doi:10.1007/978-1-4614-3909-7_6, Springer.

84 Wang, J., Zhang, L., Dai, A. et al. (2007). A near-global, 2-hourly data set of atmospheric precipitable water from ground-based GPS measurements. *J. Geophys. Res.* 112: D11. https://doi.org/10.1029/2006JD007529.

85 Smith, E. and Weintraub, S. (1953) The constants in the equation for atmospheric refractive index at radio frequencies. *Proc. IRE*, pp. 1035–1037.

86 Essen, L. and Froome, K. (1951) The refractive indices and dielectric constants of air and its principal constituents at 24,000 Mc/s. *Communication from the National Physical Laboratory*.

87 Essen, L. and Froome, K. (1963). 13th International Geodesy Association General Assembly. *Bulletin Geodesique* 70: 390.

88 Thayer, D. (1974). An improved equation for the radio refractive index of air. *Radio Science* 9: 803–807.

89 Hasegawa, S. and Stokesberry, D. (1975). Automatic digital microwave hygrometer. *Rev. Sci. Instrum.* 46: 867–873.

90 Bevis, M., Businger, S., Chiswell, S. et al. (1994). GPS meteorology: Mapping zenith wet delays onto precipitable water. *Journal of Applied Meteorology* 33: 379–386.

91 Elgered, G., Davis, J.L., Herring, T.A., and Shapiro, I.I. (1991). Geodesy by radio interferometry: Water vapour radiometry for estimation of the wet delay. *J. Geophys. Res.* 96: 6541–6555.

92 Vedel, H., Mogensen, K., and Huang, X.Y. (2001). Calculation of Zenith delays from meteorological data comparison of NWP model, radiosonde and GPS delays. *Phys. Chem. Earth* 26: 497–502.

93 Van Malderen, R., Brenot, H., Pottiaux, E. et al. (2014). A multi-site intercomparison of integrated water vapour observations for climate change analysis. *Atmos. Meas. Tech.* 7: 2487–2512. Https://doi.org/10.5194/amt-7-2487-2014.

94 Yang, X., Sass, B., Elgered, G. et al. (1999). A comparison of precipitable water vapour estimates by an NWP simulation and GPS observations. *J. Appl. Meteor.* 38: 941–956.

95 Behrend, D., Haas, R., Pino, D. et al. (2002). MM5 derived ZWDs compared to observational results from VLBI. *GPS and WVR. Phys. Chem. Earth* 27: 301–308.

96 Pacione, R., Fionda, E., Ferrara, R. et al. (2002). Comparison of atmospheric parameters derived from GPS. *VLBI and a ground-based microwave radiometer in Italy. Phys. Chem. Earth* 27: 309–316.

97 Haase, J., Ge, M., Vedel, H., and Calais, E. (2003). Accuracy and variability of GPS tropospheric delay measurements of water vapor in the western Mediterranean. *J. Appl. Meteor.* 42: 1547–1568.

98 Van Baelen, J., Aubagnac, J.P., and Dabas, A. (2005). Comparison of near-real-time estimates of integrated water vapor derived with GPS, radiosondes, and microwave radiometer. *J. Atmos. Ocean. Tech.* 22 https://doi.org/10.1175/JTECH-1697.1.

99 Bock, O., Bouin, M.N., Walpersdorf, A. et al. (2007). Comparison of ground-based GPS precipitable water vapour to independent observations and NWP model reanalyses over Africa. *Q. J. Roy. Meteor. Soc.* 133: 2001–2027. https://doi.org/10.1002/qj.185.

100 Palm, M., Melsheimer, C., Noël, S. et al. (2010). Integrated water vapor above Ny Ålesund, Spitsbergen: A multi-sensor intercomparison. *Atmos. Chem. Phys.* 10: 1215–1226. Https://doi.org/10.5194/acp-10-1215-2010.

101 Schneider, M., Romero, P.M., Hase, F. et al. (2010). Continuous quality assessment of atmospheric water vapour measurement techniques: FTIR, Cimel, MFRSR, GPS, and Vaisala RS92. *Atmos. Meas. Tech.* 3: 323–338. https://doi.org/10.5194/amt-3-323-2010.

102 Buehler, S.A., Östman, S., Melsheimer, C., Holl, G., Eliasson, S., John, V.O., Blumenstock, T., Hase, F., Elgered, G., Raffalski, U., Nasuno, T., Satoh, M., Milz, M., and Mendrok, J. (2012) A multi-instrument comparison of integrated water vapour measurements at a high latitude site. *Atmos. Chem. Phys.*, 12, 10925–10943, doi.org/10.5194/acp-12-10925-201.

103 Lafore, J., Stein, J., Asencio, N. et al. (1998). The Meso-NH atmospheric simulation system. *Part I: Adiabatic formulation and control simulations. Ann. Geophysicae* 16: 90–109.

104 Elósegui, P., Davis, J.L., Gradinarsky, L.P. et al. (1999). Sensing atmospheric structure using small-scale space geodetic networks. *Geophys. Res. Lett.* 26: 2445–2448.

105 Ruffini, G., Kruse, L.P., Rius, A. et al. (1999). Estimation of tropospheric zenith delay and gradients over the Madrid area using GPS and WVR data. *Geophys. Res. Lett.* 26 (4): 447–450. https://doi.org/10.1029/1998GL900238.

106 Biondi, R., Steiner, A.K., Kirchengast, G., and Rieckh, T. (2015). Characterization of thermal structure and conditions for overshooting of tropical and extratropical cyclones with GPS radio occultation. *Atmos. Chem. Phys.* 15: 5181–5193. Https://doi.org/10.5194/acp-15-5181-2015.

107 Jin, S., Feng, G.P., and Gleason, S. (2011). Remote sensing using GNSS signals: Current status and future directions. *Adv. Space Res.* 47 (10): 1645–1653. Https://doi.org/10.1016/j.asr.2011.01.036.

108 Bock, O., Bouin, M.N., Doerflinger, E. et al. (2008). West African Monsoon observed with ground-based GPS receivers during African Monsoon Multidisciplinary Analysis (AMMA). *J. Geophys. Res.* 113: 1984–2012. https://doi.org/10.1029/2008JD010327.

109 Adams, D.K., Gutman, S.I., Holub, K.L., and Pereira, D.S. (2013). GNSS observations of deep convective time scales in the Amazon. *Geophys. Res. Lett.* 40: 2818–2823. https://doi.org/10.1002/grl.50573.

110 Walpersdorf, A., Calais, E., Haase, J., Eymard, L., Desbois, M., and Vedel, H. (2001) Atmospheric gradients estimated by GPS compared to a high resolution Numerical Weather Prediction (NWP) model. *Phys. Chem. Earth*, pp. 147–152.

111 Liou, Y.A. and Huang, C.Y. (2000). GPS observations of PW during the passage of a typhoon. *Earth Planets Space* 52: 709–712.

112 Cucurull, L., Vilà, J., and Rius., A. (2002) Zenith total delay study of a Mesoscale Convective System: GPS observations and fine-scale modeling. *Tellus*, 54 (A), 138–147.

113 Iwabuchi, T., Miyazaki, S., Heki, K. et al. (2003). An impact of estimating tropospheric delay gradients on tropospheric delay estimations in the summer using the Japanese nationwide GPS array. *J. Geophys. Res.* 108 (D10).

114 Delrieu, G., Ducrocq, V., Gaume, E., Nicol, J., Payrastre, O., Yates, E., Kirstetter, P.E., Andrieu, H., Ayral, P.A., Bouvier, C., Creutin, J.D., Livet, M., Anquetin, S., Lang, M., Neppel, L., Obled, C., Parent-du Châtelet, J., Saulnier, G.M., Walpersdorf, A., and Wobrock, W. (2005) The catatrophic flash-flood event of 8–9 September 2002 in the Gard Region, France : A first case study for the Cévennes-Vivarais Mediterranean Hydrometeorological Observatory. *J. Hydrometeorol.*, pp. 34–51.

115 Huet, P., Martin, X., Prime, J., Foin, P., Laurain, C., and Cannard, P. (2003) Retour d'expérience des crues de Septembre 2002 dans les Départements du Gard, de l'Hérault, du Vaucluse, des Bouches du Rhône, de l'Ardèche et de la Drome, report, 133 pp, L'Inspection Gen. de l'Environ., Minist. de l'Ecol. et du Develop. Durable, Paris. (Available at http://www.side.developpement-durable.gouv.fr/Default/doc/SYRACUSE/71868), in French.

116 Chancibault, K., Anquetin, S., Ducrocq, V., and Saulnier, G.M. (2006). Hydrological evaluation of high resolution precipitation forecasts of the Gard Flash-Flood (8–9 September 2002). *Q. J. Roy. Meteor. Soc.* 132: 1091–1117. https://doi.org/10.1256/qj.04.164.

117 Seko, H., Shimada, S., Nakamura, H., and Kato, T. (2000). Three-dimensional distribution of water vapor estimated from tropospheric delay of GPS data in a mesoscale precipitation system of the Baiu front. *Earth Planets Space* 52: 927–933.

118 Hirahara, K.A. (2000). Local GPS Tropospheric Tomography. *Earth Planets Space* 52: 935–939.

119 Gradinarsky, L.P. and Jarlemark, P. (2004). Ground-Based GPS Tomography of water vapor: Analysis of simulated and real data. *J. Met. Soc. of Japan* 82: 551–560.

120 Champollion, C., Masson, F., Bouin, M.N. et al. (2005). GPS Water Vapour Tomography: First results from the ESCOMPTE field experiment. *Atmos. Res* 74: 253–274. Https://doi.org/10.1016/j.atmosres.2004.04.003.

121 Champollion, C., Flamant, C., Bock, O. et al. (2009). Mesoscale GPS tomography applied to the 12 June 2002

convective initiation event of IHOP 2002. *Q. J. Roy. Meteor. Soc.* 135: 645–662. https://doi.org/10.1002/qj.386.

122 Bastin, S., Champollion, C., Bock, O. et al. (2005). On the use of GPS tomography to investigate water vapor variability during a Mistral/sea breeze event in southeastern France. *Geophys. Res. Lett.* 32 (L05): 808. https://doi.org/10.1029/2004GL021907.

123 Bastin, S., Champollion, C., Bock, O. et al. (2007). Diurnal cycle of water vapor as documented by a dense GPS network in a coastal area during ESCOMPTE IOP2. *Amer. Meteor. Soc.* 46: 167–182. Https://doi.org/10.1175/JAM2450.1.

124 Troller, M., Geiger, A., Brockmann, E. et al. (2006). Tomographic determination of the spatial distribution of water vapour using GPS observations. *Adv. Space Res.* 37: 2211–2217. https://doi.org/10.1016/j.asr.2005.07.002.

125 Nilsson, T., Gradinarsky, L., and Elgered, G. (2007). Water vapour tomography using GPS phase observations: Results from the ESCOMPTE experiment. *Tellus* 59: 674–682. https://doi.org/10.1111/j.1600-0870.2007.00247.x.

126 Reverdy, M., Van Baelen, J., Walpersdorf, A., Dick, G., Hagen, M., and Richard, E. (2009) Water vapour field retrieval with tomography software. *Ann. Meteorol.*, 44, 144–145. Deutscher Wetterdienst: Offenbach. http://www.pa.op.dlr.de/icam2009/extabs.

127 Bender, M., Dick, G., Ge, M. et al. (2011). Development of a GNSS water vapour tomography system using algebraic reconstruction techniques. *Adv. Space Res.* 47 (10): 1704–1720. Http://doi.org/10.1016/j.asr.2010.05.034.

128 Perler, D., Geiger, A., and Hurter, F. (2011). 4D GPS water vapor tomography: new parameterized approaches. *J. Geod.* 85: 539–550. https://doi.org/10.1007/s00190-011-0454-2.

129 Notarpietro, R., Cucca, M., Gabella, M., and Perona, G. (2011). Tomographic reconstruction of wet and total refractivity fields from GNSS receiver networks. *Adv. Space Res.* 47 (5): 898–912. https://doi.org/10.1016/j.asr.2010.12.025.

130 Van Baelen, J., Reverdy, M., Tridon, F. et al. (2011). On the relationship between water vapour field evolution and precipitation systems lifecycle. *Q. J. Roy. Meteor. Soc.* 137: 204–223. https://doi.org/10.1002/qj.785.

131 Manning, T., Zang, K., Rohm, W. et al. (2012). Detecting severe weather using GPS Tomography: An Australian case study. *J. Glob. Pos. Systems* 11 (1): 58–70. https://doi.org/10.5081/jgps.11.1.58.

132 Rohm, W. (2013). The ground GNSS tomography – unconstrained approach. *Adv. Space Res.* 51: 501–513. Https://doi.org/10.1016/j.asr.2012.09.021.

133 Rohm, W., Zhang, K., and Bosy, J. (2014). Limited constraint, robust Kalman filtering for GNSS troposphere tomography. *Atmos. Meas. Tech.* 7: 1475–1486. Https://doi.org/10.5194/amt-7-1475-2014.

134 Bender, M., Stosius, R., Zus, F. et al. (2011). GNSS water vapour tomography - Expected improvements by combining GPS, GLONASS and Galileo observations. *Adv. Space Res.* 47 (5): 886–897. Http://doi.org/10.1016/j.asr.2010.09.011.

135 Ding, W., Teferle, F.N., Kazmierski, K. et al. (2017). An evaluation of real-time troposphere estimation based on GNSS Precise Point Positioning. *J. Geophys. Res.* 122: 2779–2790. https://doi.org/10.1002/2016JD025727.

136 Guerova, G., Jones, J., Douša, J. et al. (2016). Review of the state of the art and future prospects of the ground-based GNSS meteorology in Europe. *Atmos. Meas. Tech.* 9: 5385–5406. Https://doi.org/10.5194/amt-9-5385-2016.

137 Braun, J., Rocken, C., and Ware, R. (2001). Validation of line-of-sight water vapor measurements with GPS. *Radio Science* 36: 459–472. https://doi.org/10.1029/2000RS002353.

138 Kačmařík, M., Douša, J., Dick, G. et al. (2017). Inter-technique validation of tropospheric slant total delays. *Atmos. Meas. Tech.* 10: 2183–2208. Https://doi.org/10.5194/amt-10-2183-2017.

139 Zus, F., Bender, M., Deng, Z. et al. (2012). A methodology to compute GPS slant total delays in a numerical weather model. *Radio Science* 47: RS2018. https://doi.org/10.1029/2011RS004853.

140 Zus, F., Dick, G., Douša, J. et al. (2014). The rapid and precise computation of GPS slant total delays and mapping factors utilizing a numerical weather model. *Radio Science* 49: 207–216. https://doi.org/10.1002/2013RS005280.

141 Larson, K.M. (2013). A new way to detect volcanic plumes. *Geophys. Res. Lett.* 40: 2657–2660. https://doi.org/10.1002/grl.50556.

142 Houlié, N., Briole, P., Nercessian, A., and Murakami, M. (2005). Sounding the plume of the 18 August 2000 eruption of Miyakejima volcano (Japan) using GPS. *Geophys. Res. Lett.* 32 (L05): 302. https://doi.org/10.1029/2004GL021728.

143 Aranzulla, M., Cannavò, F., Scollo, S. et al. (2013). Volcanic ash detection by GPS signal. *GPS Solutions* 17 (5): 485–497. https://doi.org/10.1007/s10291-012-0294-4.

144 Grapenthin, R., Freymueller, J.T., and Kaufman, A.M. (2013). Geodetic observations during the 2009 eruption of Redoubt Volcano. *Alaska. J. Volcanol. Geotherm. Res.* 259: 115–132. https://doi.org/10.1016/j.jvolgeores.2012.04.021.

145 Aranzulla, M. and Puglisi, G. (2015). GPS tomography tests for DinSAR applications on Mt. *Etna. Ann. Geophys.* 58 (3): S0329. https://doi.org/10.4401/ag-6750.